Effects of Stress and Friction Heterogeneity on Spatiotemporal Complexity of Seismic and Aseismic Slip on Strike-Slip Faults

Jeena Yun[1], Alice-Agnes Gabriel[1,2], Dave A. May[1], and Yuri Fialko[1]

[1]Scripps Institution of Oceanography, University of California San Diego, La Jolla, CA, USA
[2]Department of Earth and Environmental Sciences, Ludwig-Maximilians Universität München, Munich, Germany

Key Points:

- Creep patches within seismogenic zone can generate stress heterogeneity and variable hypocenter depths in 2D models of strike-slip faults.
- We find that the ratio of seismogenic zone width to nucleation size is not the only factor controlling slip complexity.
- Models using slip law produce fewer partial ruptures, smaller stress drops, and lower peak slip rates compared to models using aging law.

Corresponding author: Jeena Yun, j4yun@ucsd.edu

Abstract

Numerical and laboratory models of earthquake cycles on faults governed by rate-and-state friction often show cycle-invariant behavior, while natural faults exhibit considerable variability in slip history. Possible explanations include heterogeneities in fault stress and frictional properties. We investigate how various types of heterogeneity in simulations of quasi-dynamic sequences of seismic and aseismic slip affect rupture complexity, hypocenter location, and slow slip events (SSEs). We model a 2D vertical strike-slip fault and study the roles of self-affine fractal heterogeneities in normal stress, rate-and-state parameter $(a - b)$, and characteristic slip-weakening distance, as well as the effects of a low-rigidity fault zone. We find that only a combination of heterogeneous parameters introduces variability in the modeled rupture extent, hypocenter depth, and recurrence interval. In particular, variable hypocenter depths require creeping patches within the velocity-weakening seismogenic zone. A low-rigidity fault zone adds little to slip complexity. Slip law simulations produce fewer partial ruptures, smaller stress drops, and lower peak slip rates compared to aging law simulations. We show that the ratio of the seismogenic zone thickness to nucleation size does not entirely predict slip complexity. The most complex aging law model, combining multiple heterogeneities, features system-size earthquakes preceded by cascades of partial ruptures and spontaneous SSEs. For such models, a transition from aperiodic to quasi-regular regimes requires more cycles than is typically needed to erase the effect of initial conditions. These results highlight the importance of heterogeneity in reproducing natural fault slip complexity in numerical models of earthquake sequences.

Plain Language Summary

Natural earthquakes exhibit considerable variability in their size, time, and location. In contrast, computer simulations of earthquake cycles often show cycle-invariant behavior with constant recurrence intervals and characteristic slip distributions. Possible model ingredients needed to reproduce the variable slip histories observed in nature include heterogeneities in fault properties. We investigate how various types of heterogeneity in simulations of sequences of earthquakes affect rupture complexity. We find that only a combination of multiple heterogeneities introduces variability in the modeled earthquake size, location, and recurrence interval. In particular, variable hypocenter depths require areas of stable creep within the seismogenic zone. Including a layer of less stiff material near the fault adds little to slip complexity. The most complex model in this study, combining multiple heterogeneities, features non-repeating cycles of large earthquakes preceded by a cascade of smaller foreshocks. However, the complexity transitions to periodic cycles after ∼1700 years of simulation time, suggesting heterogeneity-induced variability in modeled slip history may only be transient. Our results also suggest that 3D effects may be important for producing and maintaining spatiotemporal complexity in fault slip.

1 Introduction

The theory of rate-and-state friction (RSF; Dieterich, 1979; Ruina, 1983) is widely used to model seismic and aseismic slip on geological faults (e.g., Barbot et al., 2012; Erickson et al., 2020; Jiang & Lapusta, 2016; Tse & Rice, 1986). Simulations of earthquake sequences on faults obeying RSF successfully reproduce many aspects of the observed behavior of natural faults, including stick-slip (e.g., V. C. Li & Rice, 1987; Lapusta et al., 2000), afterslip (Barbot et al., 2009; Helmstetter & Shaw, 2009; Perfettini & Avouac, 2007; K. Wang & Fialko, 2014), interseismic creep (Kaneko et al., 2013; Lindsey & Fialko, 2016), the Gutenberg-Richer and Omori laws (Beall et al., 2022; Cattania, 2019; Dieterich, 1994; Ito & Kaneko, 2023), and earthquake triggering (Luo & Liu, 2019; Perfettini et al., 2003a, 2003b; Wei et al., 2018).

However, models of sequences of earthquakes and aseismic slip (SEAS) on faults governed by RSF often exhibit cycle invariance, whereby the recurrence intervals and slip patterns become constant following some initial "spin-up phase" in which the effects of initial conditions are erased (e.g., Erickson et al., 2020; Rice, 1993; Tse & Rice, 1986; S. Wang, 2024), particularly when no heterogeneity is assumed. Such models also exhibit a limited range of earthquake nucleation depths (e.g., Barbot, 2019; Cattania, 2019; Erickson et al., 2023; Lapusta & Rice, 2003). This is in contrast to the observed seismicity patterns on natural faults that are characterized by highly irregular recurrence intervals and a wide distribution of hypocenter locations throughout the seismogenic zone (e.g., Jin & Fialko, 2020; Ross et al., 2020; Waldhauser & Schaff, 2008).

Previous studies reproduced the observed complex slip behavior by introducing inherent discreteness, e.g., by using numerical grids that are coarser than the characteristic nucleation size (e.g., Ben-Zion & Rice, 1995; Rice, 1993; Rice & Ben-Zion, 1996; Ziv & Cochard, 2006), or modifying constitutive parameters to facilitate nucleation (e.g., Cochard & Madariaga, 1996; Shaw & Rice, 2000). In continuum models, spatiotemporal complexity of slip can arise from various heterogeneities, including spatially variable frictional properties (Hillers et al., 2007; Jiang & Fialko, 2016; M. Li et al., 2025; Luo & Ampuero, 2018; Molina-Ormazabal et al., 2023), elastic moduli (Y. Huang et al., 2014; Idini & Ampuero, 2020; Thakur et al., 2020), and fault geometry (Cattania & Segall, 2021; Ozawa & Ando, 2021; Tal & Gabrieli, 2024; Yin et al., 2023). Models that allow for intermingled patches of stable and unstable slip have shown that interactions between these patches may also enhance slip complexity (J. Huang & Turcotte, 1990; Kato, 2020; Nakata et al., 2011) and produce realistic foreshock migration patterns and Omori-type aftershock sequences (Dublanchet et al., 2013; Ito & Kaneko, 2023; Luo & Ampuero, 2018). However, in many previous studies, the heterogeneities are assumed to be regularly spaced and piece-wise constant (e.g., Ito & Kaneko, 2023; Kato, 2020; Molina-Ormazabal et al., 2023) or randomly distributed (e.g., Galvez et al., 2020; Hillers et al., 2006), often with bimodal strength distributions. While the spatial distribution of subsurface frictional properties remains poorly constrained, a deeper understanding of how strongly varying heterogeneous fault properties affect the complexity of earthquake cycles is warranted.

Alternatively, it was shown that increases in slip complexity can result from decreases in the critical length scale of the nucleation process relative to the characteristic fault size (Cattania, 2019; Erickson et al., 2011; Herrendörfer et al., 2015; Y. Liu & Rice, 2007; Nie & Barbot, 2022). Numerical models show less regular cycles of earthquakes for smaller characteristic nucleation size, with the emergence of partial ruptures (e.g., Barbot, 2019; Cattania & Segall, 2019; Lapusta et al., 2000) and realistic earthquake statistics such as the Omori-type aftershock decay or the frequency-magnitude relation (e.g., Cattania, 2019). However, the respective models still exhibit a narrow range of hypocenter locations, mostly limited to the edges of the seismogenic zone (e.g., Barbot, 2019; Lapusta & Rice, 2003).

Complexity in rupture evolution in SEAS models can additionally be introduced by various other sources. For example, complex fault geometry, such as curved or rough fault surfaces (Ozawa & Ando, 2021; Perez-Silva et al., 2022; Yin et al., 2023) and effects of pore fluids (e.g., Zhu et al., 2020) have been shown to produce ruptures of variable sizes, varying nucleation locations, and aseismic transients. Incorporating full elastodynamics may facilitate more variable system dynamics, by accounting for the stress transfer via radiated seismic waves (e.g., Thakur et al., 2020). Introducing bulk inelasticity has been shown to produce complex rupture evolution (e.g., Abdelmeguid et al., 2024; Mia et al., 2023). However, many SEAS studies adopt a quasi-dynamic approach (Eq. (2)) with a simple, planar fault embedded in a purely elastic medium, omitting fluid interactions. In this study, we seek to identify mechanisms that can generate considerable complexity in models that admit several simplifying assumptions. We discuss po-

tential limitations of omitting physically relevant factors such as inertia (Sections 4.1 & 4.5).

The largely empirical RSF framework involves a choice of the functional form of the so-called evolution law for the state variable (e.g., Ampuero & Rubin, 2008; Dieterich, 1979; Ruina, 1983). The two most common choices are the aging law (Dieterich, 1979) and the slip law (Ruina, 1983), but other forms of the evolution law were proposed as well (e.g., Kato & Tullis, 2001; Linker & Dieterich, 1992; Nagata et al., 2012; Sato et al., 2025; Yoshida et al., 2020). Different formulations are meant to explain different aspects of available experimental data. For example, the aging law well captures the time-dependent healing of the rock surface in slide-hold-slide and stick-slip experiments (e.g., Beeler et al., 1994; Dieterich & Kilgore, 1994; Mitchell et al., 2015, 2016), while the slip law seemingly better accounts for the evolution of friction in velocity stepping experiments with large velocity changes (e.g., Ampuero & Rubin, 2008; Bayart et al., 2006; Pignalberi et al., 2024). These empirical laws have different intrinsic length scales and predict different slip evolutions away from the steady state (Ampuero & Rubin, 2008). How various choices of the state evolution law may affect the complexity of the system behavior and a fault's response to external stress perturbations is not well understood.

In this study, we investigate the effects of various types of heterogeneity on rupture complexity, hypocenter location, and aseismic transients in simulated earthquake and aseismic slip sequences. SEAS simulations empowered by high-performance computing enable more realistic parameterization, extensive parameter space exploration, and volume-discretized methods, addressing key knowledge gaps despite high computational costs (e.g., Taufiqurrahman et al., 2023; Uphoff et al., 2023; Erickson & Dunham, 2014; D. Liu et al., 2020; Pranger, 2020; Thakur et al., 2020). We perform a suite of 2D quasi-dynamic SEAS simulations on a planar vertical strike-slip fault under the antiplane strain approximation, incorporating different heterogeneities on and off the fault (Sections 3.1-3.3) and using two different state variable evolution laws (Section 3.4). We document key features of the most complex models obtained in this study, including cascades of ruptures, emergence of spontaneous slow slip events, and quasi-chaotic earthquake sequences (Section 3.2). We find that heterogeneity in a single parameter is insufficient to sustain complex rupture behavior in a 2D quasi-dynamic framework. Moreover, models with comparable ratios of the seismogenic fault width to characteristic nucleation length scale can exhibit markedly different levels of system complexity (Section 4.2). Diversity in hypocenter depths is strongly affected by the presence of creeping patches within the seismogenic zone, and less so by a low-rigidity fault zone. These results provide insights into how the system behavior, including the rupture characteristics, depends on various heterogeneities in material properties and field variables, as well as different assumed evolution laws. In a companion paper, we use the complex multi-cycle simulations developed here, incorporating heterogeneous material properties, to investigate the triggering potential of rate-and-state friction faults perturbed by static and dynamic stress changes from nearby earthquakes (Yun et al., 2025a).

2 Methods

2.1 Models of Earthquake Sequences on Faults governed by RSF

We use the open-source code *Tandem* (Uphoff et al., 2023) to perform 2D antiplane strain quasi-dynamic SEAS simulations on a vertical strike-slip fault embedded in an elastic halfspace (Fig. 1a). *Tandem* is based on a symmetric interior penalty discontinuous Galerkin method and is optimized for high-performance computing. *Tandem* uses the regularized version of the rate-and-state friction formulation (Lapusta et al., 2000):

$$F(\|\boldsymbol{V}\|,\theta) = a\sinh^{-1}\left[\frac{\|\boldsymbol{V}\|}{2V_0}\exp\left(\frac{f_0 + b\ln\left(V_0\theta/D_{RS}\right)}{a}\right)\right], \tag{1}$$

where F is the instantaneous friction coefficient, $\|\boldsymbol{V}\|$ is the Euclidean norm of the slip rate vector $\boldsymbol{V}$, θ is the state variable, a, b are the rate-and-state parameters for direct and evolution effect, respectively, D_{RS} is the characteristic state evolution distance, V_0 is the reference slip rate, and f_0 is the reference friction coefficient. All SEAS model parameters used in this study are summarized in Table 1.

The sign of $(a-b)$ determines the stability of the system. An increase in sliding velocity leads to a drop of static friction when $a-b<0$, promoting instability, which is referred to as velocity-weakening (VW) behavior. Conversely, static friction increases when $a-b>0$, suppressing instability, which is defined as velocity-strengthening (VS) behavior. In this study, we include shallow and deep VS regions surrounding a central VW zone, representing a 10-km-wide seismogenic zone (Fig. 1a). The rate-and-state fault is loaded from the bottom creeping zone and the far boundary with a constant velocity (V_{pl}) of 10^{-9} m/s $\approx$ 30 mm/yr, corresponding to the long-term fault slip rate.

In quasi-dynamic simulations, the inertial effect is approximated by a radiation damping term $\eta\boldsymbol{V}$ (Rice, 1993):

$$-\boldsymbol{\tau} = \sigma_n F(\|\boldsymbol{V}\|,\theta)\frac{\boldsymbol{V}}{\|\boldsymbol{V}\|} + \eta\boldsymbol{V}, \tag{2}$$

where $\eta = \mu/2c_s$ is half of the shear-wave impedance with shear modulus μ and shear-wave speed c_s, and $\boldsymbol{\tau}$ and σ_n are shear and normal stresses on the fault, respectively. Although quasi-dynamic models do not capture all aspects of fully dynamic solutions, particularly in the presence of geometric or rheological barriers (e.g., Kroll et al., 2023; Lambert & Lapusta, 2021), they produce qualitatively comparable slip patterns at considerably reduced computational cost (Lapusta & Rice, 2003; Rice & Ben-Zion, 1996; Thomas et al., 2014). We discuss the potential effect of the quasi-dynamic approximation in more detail in Section 4.1.

The evolution of the state variable θ is governed by an ordinary differential equation. We explore the two most common end-members, the aging law (Dieterich, 1979):

$$\frac{d\theta}{dt} = 1 - \frac{\|\boldsymbol{V}\|\theta}{D_{RS}}, \tag{3}$$

and the slip law (Ruina, 1983):

$$\frac{d\theta}{dt} = -\frac{\|\boldsymbol{V}\|\theta}{D_{RS}}\ln\left(\frac{\|\boldsymbol{V}\|\theta}{D_{RS}}\right). \tag{4}$$

We set the initial value for the state variable (θ^0) to be consistent with the background shear stress (τ^0) and initial slip rate (V_{init}):

$$\theta^0 = \frac{D_{RS}}{V_0}\exp\left\{\frac{a}{b}\ln\left[\frac{2V_0}{V_{\mathrm{init}}}\sinh\left(\frac{\tau^0-\eta V_{\mathrm{init}}}{a\sigma_n}\right)\right] - \frac{f_0}{b}\right\}. \tag{5}$$

The ratio of the length of the seismogenic fault (W; Table 1) to the critical nucleation size is known to affect the complexity of the earthquake sequence. For 2D antiplane simulations using the aging law (with $0.5 < a/b < 1$), the critical nucleation size (L_∞) can be expressed as follows (Rubin & Ampuero, 2005):

$$L_\infty = \frac{2}{\pi}\frac{\mu b D_{RS}}{\sigma_n(b-a)^2}. \tag{6}$$

There is no equivalent analytical form of the critical nucleation size for the slip law, as the nucleation zone continuously shrinks under the slip law formulation (Ampuero & Rubin, 2008). Thus, we only compare the W/L_∞ ratios among aging law models. The critical nucleation size also controls the grid size, as the former needs to be resolved by the

model. A detailed description of different model resolution requirements for each evolution law is provided in Supplementary Section S1.

We use adaptive time stepping handled by the software PETSc (Abhyankar et al., 2014; Balay et al., 1997, 2019) with a fourth-order embedded fifth-order Dormand-Prince scheme Runge-Kutta method.

2.2 Fractal Heterogeneities

As one realization of the poorly constrained distribution of heterogeneity in natural fault zone properties, we assume a self-affine fractal variation that captures the scale-dependent variability observed, e.g., in fault roughness (Candela et al., 2012; Lee & Bruhn, 1996; Maurer, 2024; Renard et al., 2006). We introduce band-limited self-affine fractal variations to the effective normal stress (σ_n), rate-and-state parameters ($a-b$), and the characteristic state evolution distance (D_{RS}). The 1D fractal distributions are characterized by the power spectral density $P(k)$ as follows (Andrews & Barall, 2011; Dunham et al., 2011):

$$P(k) \propto k^{-(2H+1)} \tag{7}$$

with the wavenumber k and the Hurst exponent H. The Hurst exponent $H = 1$ results in a self-similar fractal distribution, while $0 \leq H < 1$ produces a self-affine distribution. For natural faults, H is typically assumed to vary between 0.4 and 0.8 (Renard & Candela, 2017). We assume $H = 0.7$ for most of the fractal profiles used in this study (Cattania & Segall, 2021). We also evaluate the effects of higher values of the Hurst exponent ($H = 1.9$) on rupture evolution (see Supplementary Section S3). The fractal variation is limited between minimum (λ_{min}) and maximum (λ_{max}) wavelengths. We explore a wide range of λ_{min} from 25 m (comparable to the critical nucleation size) to 750 m and λ_{max} from 2.5 km to 10 km (comparable to W) to identify values of λ_{min} and λ_{max} that produce most diversity in both rupture sizes (e.g., occurrence of both partial ruptures and system-size events) and hypocenter depths (i.e., widely distributed nucleation locations within the seismogenic zone).

We use a Fourier transform method (Andrews & Barall, 2011; Shi & Day, 2013) to generate the fractal profile and take an amplitude-to-wavelength ratio $\alpha = 10^{-2}$ to scale the root-mean-square amplitude of the profile (Dunham et al., 2011). Since our model fault is 1D, the α value refers to variations in the direction perpendicular to slip. All fractal variations are tapered outside the seismogenic zone by scaling their amplitude by the distance from the nearest VW region. The fractal amplitudes are then converted into variations of parameters by applying scaling factors that match the order of magnitude of each parameter (Table S1). For example, the fractal effective normal stress profile is obtained by scaling the fractal amplitude by $(\rho_c - \rho_w)g$, where $\rho_c = 2670$ kg/m^3 is density of crust, $\rho_w = 1000$ kg/m^3 is density of water, and $g = 9.8$ m/s^2 is the acceleration due to gravity. Since the fractal heterogeneity has a mean of zero, the average value for each parameter (i.e., $\overline{\sigma_n}$, $\overline{a-b}$, and $\overline{D_{RS}}$) remains the same for both fractal (red solid lines in Figs. 1b-d) and non-fractal (grey dashed lines in Figs. 1b-d) distributions. All fractal heterogeneity models explored in this study are summarized in Table S1 and shown in Figure S1.

Our models do not explicitly account for fault roughness or fault geometric effects (e.g., Cattania & Segall, 2021; Ozawa & Ando, 2021; Tal & Gabrieli, 2024), but instead prescribe heterogeneous stress and strength conditions on a planar fault. These may differ from rough-fault models where shear drag can preserve heterogeneity throughout the cycle (Dunham et al., 2011; Shi & Day, 2013). Given our 2D antiplane strain model assumptions, incorporating true geometric roughness is beyond the scope of this study.

2.3 Event Detection and Classification

We implement an automated event detection and classification algorithm to systematically compare the event time and hypocenter locations across different models. A seismic event is identified when the peak slip rate along the fault exceeds a threshold velocity, which varies between 0.01 m/s and 0.2 m/s, for longer than 0.5 s at more than one of the evaluation points, which are spaced every 200 m along the fault. An event is disregarded if the difference between the maximum and minimum peak slip rates during the event is less than 15% of the threshold velocity to eliminate minor fluctuations in slip rate. A detailed description of the post-processing procedures is provided in Supplementary Section S2.

A 'system-size earthquake' is defined as an event that ruptures a length greater than 10 km (i.e., the entire seismogenic zone), while all other events are denoted 'partial rupture events' hereafter. A 'leading foreshock' is defined as the first partial rupture event in a sequence that eventually leads to a system-size earthquake.

2.4 Assessing the Level of Complexity

To quantitatively evaluate the degree of complexity across different models, we introduce a 'complexity score' based on three aspects of slip history: 1) how widely the hypocenters of system-size earthquakes are distributed as a function of depth, 2) the periodicity of the sequence, and 3) whether partial ruptures exist and if so, how diverse their sizes are. Each aspect is scored between 0 and 1, and the combined complexity score, the sum of all three metrics, ranges from 0 to 3.

The complexity score for hypocenter depth heterogeneity of system-size earthquakes is computed based on the histogram of hypocenter depths of system-size earthquakes. We count the number of bins n along depth (0.5 km interval) that contain at least one system-size earthquake hypocenter. To ensure a score of zero when all events occur at the same depth, we subtract 1 from the bin count ($n-1$). The respective score is then $(n-1)/(N-1)$, where N is the maximum value of n in all of the tested models.

The complexity score for periodicity is computed from the standard deviation of indices for the nearest system-size events with hypocenter depths less than 0.5 km apart. This standard deviation is normalized to 1 to provide the final score.

Lastly, the complexity score for heterogeneity in partial rupture events is computed from the standard deviation of rupture lengths among partial rupture events. If no partial rupture events are present, the score is assigned a value of zero, and the resulting score is normalized to 1.

3 Results

3.1 Models with Heterogeneity in a Single Parameter

We explore a range of heterogeneities to yield a SEAS model with realistic variability in both event size and hypocenter depth distribution. The W/L_∞ ratio in these models varies with depth, due to the fractal spatial distribution of parameters. This study covers the range of maximum W/L_∞ values between 5 and 400 (Fig. 9). All SEAS models explored in this study are summarized in Table S2.

Using the aging law, we find that neither heterogeneity in a single parameter (Figs. 2 & 3) nor the presence of a low-rigidity fault zone (Fig. 5) alone is sufficient to introduce the desired complexity. Most of the models with heterogeneity in a single parameter exhibit characteristic cycles and hypocenters located only at the periphery of the seismogenic zone, similar to results from models that do not assume any heterogeneity (e.g.,

Lapusta & Rice, 2003; Lindsey & Fialko, 2016). We also tested models in which normal stress increases with depth with superimposed fractal heterogeneity (Fig. 3c), but the cycles remained repeatable, with nucleation limited to the bottom edge of the seismogenic zone, where the critical nucleation size (L_∞, Eq. (6)) is the smallest. It is expected that depth-dependent normal stress favors nucleation at the base of the seismogenic zone but adds little to complexity (e.g., Zhang et al., 2006).

Two notable exceptions to the general lack of complexity in single-heterogeneity models are a model with a variable $(a-b)$ profile featuring VS-VW transitions (model R1; Fig. 2b) and a model with heterogeneous σ_n with a larger amplitude-to-wavelength ratio, α (model N7; Fig. 3d). Introducing an $(a-b)$ profile with VS patches within the seismogenic VW region gives rise to earthquakes that nucleate at various depths within the seismogenic zone, rather than only at its periphery. Earthquakes nucleate at the boundaries of VS patches, where the stressing rate is increased due to creep on VS patches. Nucleation in the middle of the seismogenic zone is absent in other heterogeneous $(a-b)$ profiles that lack VS patches embedded within the VW layer (model R3; Fig. 2c).

In model N7, we use a larger $\alpha = 4 \times 10^{-2}$, increasing the variability in the normal stress heterogeneity. The root-mean-square normal stress variation $\Delta\sigma_{\text{rms}}$ in this model is ∼10 MPa, compared to ∼3 MPa in other models with heterogeneous σ_n. This elevated heterogeneity leads to considerably more complex rupture evolution, featuring partial ruptures, creep patches within the seismogenic zone, and spontaneous shallow and deep slow slip events (SSEs) at its base. Importantly, earthquakes in model N7 nucleate within the seismogenic zone (Fig. 3d), unlike any other models with heterogeneous σ_n. Creep patches begin to emerge during the later stages of the earthquake cycle, preceding the next system-size event, and are colocated with regions of moderately low effective normal stress (20-40 MPa). SSEs occur within the patch of the lowest σ_n (∼10 MPa; see also Section 4.6). The SSEs in model N7 load a nearby high-σ_n patch, triggering partial ruptures that in turn load another high-σ_n patch. A system-size earthquake occurs when the patch with the highest normal stress becomes sufficiently stressed by preceding SSEs and partial ruptures. These results may be comparable to those of previous models analyzing heterogeneous normal stress induced by rough surfaces and how this promotes complex rupture sequences (Cattania & Segall, 2021; Tal et al., 2018).

The lack of complexity in single-heterogeneity models is likely not related to the choice of Hurst exponent. We test two different values of H (0.7 and 1.9) and find only minor effects on rupture evolution in models with heterogeneity in D_{RS} (group D) and normal stress (group N), including minimal changes in recurrence intervals and unchanged complexity scores. The effect of different Hurst exponents is more pronounced in models with heterogeneity in $(a-b)$ (group R). A detailed discussion is provided in the Supplementary Section S3.

3.2 Models with Combined Stress and Frictional Heterogeneities

Combining an $(a-b)$ profile that includes VS patches within the seismogenic zone with heterogeneity in other model parameters, e.g., models N3R1, N3R1D1, and N3R2D1, consistently produces cycles with system-size earthquakes preceded by a cascade of partial ruptures (Figs. 4 & 6). The hypocentral depths of the system-size events are broadly distributed throughout the seismogenic zone. The maximum W/L_∞ values range from 60 to 400 (Fig. 9). Nonetheless, all these models remain quasi-periodic, with a constant nucleation depth for all system-size earthquakes in each model, respectively, although the nucleation depth may be different in different models.

When heterogeneity in all three parameters ($(a-b)$, D_{RS}, and σ_n) is combined, and the $(a-b)$ profile has large amplitude variations (as in model N3R2D1), spontaneous deep and shallow SSEs are generated (Fig. 7), consistent with observations (Rousset et al., 2019; Vavra et al., 2024; Wei et al., 2009). Deep SSEs in model N3R2D1 spatially

coincide with a small VW patch embedded within the deep VS zone. This suggests that instability is initiated at the VW patch but fails to grow into a runaway seismic rupture due to the VS barriers located above and below. Shallow SSEs occur only after a sequence of partial rupture events, presumably to relax the stress induced by the preceding sequence. The peak slip rate of the shallow SSEs is an order of magnitude lower than that of the deep SSEs (Figs. 7a-b). Both shallow and deep SSEs are often followed by a sequence of partial rupture events, similar to the observation of aseismic slip preceding small to moderate earthquakes (e.g., Linde et al., 1988; L. Huang et al., 2024; Thurber, 1996; Thurber & Sessions, 1998). A detailed discussion of the mechanism underlying SSE generation in our models is provided in Section 4.6.

We do not find a comparable level of complexity in models without heterogeneous $(a-b)$ profiles with VS patches embedded within the seismogenic zone. For example, model N3D1 (Fig. 5b) shows a relatively simple rupture evolution, in which initial heterogeneities are rapidly wiped out, approaching a periodic cycle consisting of a single partial rupture and a system-size event. This result illustrates the importance of sustained stress heterogeneity, achieved either through alternating rheological properties (e.g., VS-VW transitions) or pronounced heterogeneity (e.g., model N7), which creates variability in nucleation locations and rupture size. A more detailed discussion of the driving mechanisms controlling variations in hypocentral depth is provided in Section 4.1.

Models with combined heterogeneities in multiple parameters exhibit more complex rupture patterns compared to those with heterogeneity in only one parameter, even when frictional strength, defined as $\sigma_n(a-b)$, is the same. For example, models N3R1 and R1m share the same spatial distribution of frictional strength. However, model N3R1 includes correlated fractal heterogeneity in both σ_n and $(a-b)$ (black lines in Fig. 4a), whereas model R1m has heterogeneity only in $(a-b)$ that matches the frictional strength profile of model N3R1 (red lines in Fig. 4a). Note that the individual σ_n and $(a-b)$ profiles differ between models N3R1 and R1m, even though both are constructed to match the same $\sigma_n(a-b)$. If frictional strength alone governed system complexity, and the contributions of σ_n and $(a-b)$ could not be distinguished, the two models should evolve into an identical SEAS cycle. Despite this matched frictional strength, model N3R1 produces more variable hypocenter depths of system-size events and more variable sizes of partial ruptures compared to model R1m (Figs. 4b-c). The corresponding complexity scores (Section 2.4) are 0.7 for model N3R1 and 0.3 for model R1m, confirming that model N3R1 is more complex than model R1m. We assess differences between the two models only considering spun-up cycles, e.g., after event 20 in model N3R1 (Fig. 4b) and after event 11 in model R1m (Fig. 4c). The persistence of this difference, even after adjusting for initial conditions, indicates that the presence of a spatial stress gradient is important for producing complex rupture patterns in our models. This result is consistent with the increased complexity in model N7, which involves a larger gradient in normal stress.

Through trial-and-error, we identify one model (N12R4D4) that shows a longer, sustained aperiodicity (Fig. 6c). In this model, system-size earthquakes are consistently preceded by a cascade of partial rupture events. Spontaneous SSEs emerge at shallow and deep edges of the seismogenic zone. This model incorporates heterogeneity in both $(a-b)$ and D_{RS} with a high Hurst exponent of 1.9. The heterogeneous normal stress profile in model N12R4D4 resembles a band-limited fractal distribution with $H = 1.9$ within a limited bandwidth (500 m - 2.5 km), but contains a much richer short-wavelength component, compared to a strictly self-affine fractal distribution (grey vs. purple lines in Fig. S6). The transition from fractal to non-fractal scaling occurs at about $\lambda_{min} =$ 500 m, which is comparable to the observationally defined crossover length scale, below which the log-linear scaling of the power spectra of a rough surface becomes unreliable (Candela et al., 2012). Therefore, we take this model as representing heterogeneity with

larger roughness at short length scales. A detailed discussion of the longer-lasting complexity shown in model N12R4D4 is provided in Section 4.5.

3.3 Models with a Low Rigidity Fault Zone

We perform additional SEAS simulations adding a low-rigidity region surrounding the fault, as an analogy to damage zones developing near active faults (e.g., Chester et al., 1993; Fialko et al., 2002; Y. Huang et al., 2014; Gabriel et al., 2024). We include a rectangular low-rigidity fault zone (with rigidity μ_{FZ}), 500 m wide and 10 km deep, which tapers at the bottom end as a semi-circle with a 500 m radius (Fig. 1a).

We find that the presence of a low-rigidity fault zone has minimal impact on earthquake sequences across all considered cases in this study, which explores two different rigidity contrast values (30% and 60%; Table S2). Without the inclusion of fractal heterogeneities in the initial dynamic parameters (model FZ), the low-rigidity fault zone alone results in partial rupture events and system-size earthquakes, but the sequence remains cycle-invariant, with hypocenters located only at the bottom of the seismogenic zone.

Including a low-rigidity fault zone in models with fractal heterogeneities adds little to the complexity. For example, models N3D1FZ and N3D1 share the same fractal heterogeneity, but model N3D1FZ includes a low-rigidity fault zone ($\mu_{FZ} = 20$ GPa & $\mu = 32$ GPa), while model N3D1 has a uniformly low $\mu = 20$ GPa in the entire bulk. Both models exhibit periodic cycles without variability in hypocenter depth (Fig. 5). While model N3D1 produces partial ruptures, model N3D1FZ shows only system-size events. Similar results are observed using a different Hurst exponent. Using $H = 1.9$, models N12D4FZ and N12D4 exhibit a comparable rupture evolution, characterized by periodic cycles consisting of a partial rupture and a system-size rupture nucleating at the base of the seismogenic zone (Fig. S2).

3.4 Comparing Aging Law and Slip Law Models

We perform a suite of simulations to assess the effect of using different evolution laws. The model assuming slip law is shown in Figure 8a. This model uses the same set of parameters as used in the N3R1D1 simulation but with an increased $\overline{D_{RS}}$ of 10 mm (D_{RS} heterogeneity version 2; Table S1) to reduce the computational burden (see Supplementary Section S1). The modeled earthquake sequence (denoted as N3R1D2-S, where 'S' stands for slip law) is characterized by the repetition of a few partial rupture events at the base of the seismogenic zone, followed by a system-size earthquake in the middle of the seismogenic zone (∼5 km depth). Periodic earthquake sequences and a scarcity of smaller earthquakes are observed in model N3R1D2-S, as noted in previous studies that considered the effects of slip law (e.g., Rice & Ben-Zion, 1996; Rubin, 2008).

We produce a new aging law model using $\overline{D_{RS}} = 10$ mm (denoted model N3R1D2; Fig. 8b), for direct comparisons among different evolution laws. Models N3R1D2 and N3R1D1 differ only in the magnitude of $\overline{D_{RS}}$ (10 mm vs. 2 mm).

Model N3R1D2 shows more complex earthquake sequences with multiple partial rupture events preceding system-size earthquakes compared to the 'equivalent' slip law model (N3R1D2-S). In model N3R1D2, multiple partial rupture events are connected by a prolonged aseismic slip, forming a sequence that eventually leads to a system-size earthquake. Due to this prolonged aseismic slip, each sequence in model N3R1D2 lasts for about 21 minutes on average, much longer compared to ∼21 seconds in the N3R1D2-S model.

We find that the aging law (model N3R1D2) tends to produce larger static stress drops and peak slip rates during its system-size events compared to the slip law (model N3R1D2-S), although their differences are rather small: Model N3R1D2 and the N3R1D2-

S model have average stress drops of ∼5 MPa and ∼3 MPa, respectively, and average peak slip rates of ∼3.6 m/s and ∼3.4 m/s. Differences in stress drops and peak slip rates between models using aging and slip laws are consistent with results from previous studies (Hawthorne & Rubin, 2013; He et al., 2003; Perfettini & Ampuero, 2008; Pignalberi et al., 2024); we provide a more detailed comparison in Section 4.4.

4 Discussion

4.1 Variability in the Hypocenter Depth

Contrary to the predictions of classic SEAS models on RSF faults, which limit earthquake nucleation to the edges of the VW layer representing the seismogenic zone (Lapusta & Rice, 2003; Rice, 1993; Tse & Rice, 1986), natural faults exhibit a wide range of hypocenter depths (Melgar et al., 2023; Ross et al., 2020; Waldhauser & Schaff, 2008). In particular, in California, most earthquakes nucleate in the middle, rather than at the edges, of the seismogenic zone (Jin & Fialko, 2020).

The models presented here replicate such diverse hypocenter depths when we introduce VS patches within the seismogenic zone (Figs. 1c & 2b). This variability arises because stress concentrates at the VS-VW transitions due to creep in the VS patch (e.g., Lapusta & Rice, 2003; Lindsey & Fialko, 2016). These transitions between VS and VW also facilitate the spontaneous occurrence of deep SSEs. Although the alternation of creeping and locked regions in our models clearly creates stress heterogeneity and facilitates variability in hypocenter depth, not all VS-VW transitions accommodate nucleation. We do not observe a clear relationship between earthquake hypocenters and the size or strength of the VS patches (Fig. S3). Some VS patches that do not host nucleation, for example, a VS patch at $\sim$ 5 km depth in model R1 (Fig. S3a), instead act as rupture barriers. These patches are often small, with resistances expected to be minor based on scaling relations for uniform VS patches suggested by Kaneko et al. (2010). These results suggest that VS patches with variable sizes and strengths may alter stress conditions more effectively than uniform VS patches. Under fractally varying $(a - b)$, even small or weak VS patches may play a non-negligible role.

Another case that produces variability in hypocenter depth arises when we use heterogeneous effective normal stress with large amplitude variations, as in model N7 (Fig. 3d). In this model, system-size earthquakes nucleate in the middle of the seismogenic zone, where patches of elevated normal stress are progressively loaded by preceding SSEs or partial ruptures. This behavior contrasts with other models with heterogeneous σ_n, which fail to nucleate system-size earthquakes, even when stress heterogeneity is generated by partial ruptures (e.g., Fig. 5b). These results suggest that elevated static strength is required to enable earthquake nucleation within the seismogenic zone, not only at its periphery. In model N7, the ratio of $\Delta\sigma_{\mathrm{rms}}$ to the background normal stress level (50 MPa) is about 0.5, which is lower than the threshold of 1.1 suggested by Cattania and Segall (2021) for promoting smaller earthquakes preceding system-size earthquakes. However, the large total range of normal stress variation of ∼70 MPa (spanning from ∼10 MPa to ∼80 MPa) in this model may not be realistic. While this model confirms the role of strong normal stress variability in generating variability in nucleation location, caution is warranted when extrapolating these results to real faults.

In the context of the 2D quasi-dynamic, antiplane strain models on a planar fault presented here, no heterogeneity is capable of producing a broad distribution of event hypocenters unless it involves creeping patches (model R1) or significantly increased effective normal stress (model N7). Previous 2D quasi-dynamic, antiplane strain models exhibit similar limitations, even in models that showed variable rupture extent and realistic frequency-magnitude relationships (e.g., Barbot, 2019; Cattania, 2019). In contrast, such variability in nucleation depths is frequently observed in SEAS models with

varying assumptions. 3D models show earthquake nucleation within a central VW layer, equivalent to the seismogenic zone in our study, not only when heterogeneous fault friction is introduced (e.g., heterogeneous D_{RS}: Galvez et al., 2020; Hillers et al., 2006; heterogeneous $(a-b)$: Jiang & Lapusta, 2016) but also for relatively simple parameter setups (e.g., Lapusta & Liu, 2009). Complex fault geometries (e.g., curved fault, rough surface, multiple faults) can introduce variability in nucleation location, even without heterogeneous model parameters (e.g., Ozawa & Ando, 2021; Perez-Silva et al., 2022; Yin et al., 2023). Accounting for fluid flow and permeability evolution successfully produces earthquake swarms within the seismogenic zone as well as slow transients (Ozawa et al., 2024; Zhu et al., 2020). Incorporating inelasticity in bulk material may also introduce aperiodic cycles and clustering of earthquakes as localized plastic strain accumulation facilitates segmentation of ruptures (e.g., Abdelmeguid et al., 2024; Mia et al., 2023). The inclusion of dynamic wave propagation may introduce additional variability in nucleation locations. For example, while both Abdelmeguid et al. (2019) and Thakur et al. (2020) model 2D antiplane slip on a vertical strike-slip fault embedded in a low-rigidity fault zone, variability in hypocentral depths emerges only in the fully dynamic simulations of Thakur et al. (2020).

4.2 Control of W/L_∞ on the Slip Complexity

We systematically compare maximum and median values of W/L_∞ with the complexity scores (Section 2.4) across all aging law models (Fig. 9). Overall, the maximum W/L_∞ ratio correlates well with the combined complexity score. A larger W/L_∞ ratio tends to increase the diversity in partial rupture events (Fig. 9c), while having little impact on the periodicity (Fig. 9b) and the hypocenter depth heterogeneity of system-size earthquakes (Fig. 9a).

However, a larger W/L_∞ ratio does not always lead to a more complex model. For example, model D1 (octagons in Fig. 9) has higher median and maximum W/L_∞ ratios than model N7 (circles in Fig. 9). Yet, model D1 produces periodic cycles consisting of a partial rupture and a system-size earthquake that nucleate at a fixed depth, while model N7 produces variable hypocenter depths and SSEs. This lack of complexity in model D1, despite a higher W/L_∞ ratio compared to model N7, is likely related to the model setup differences. As discussed in Section 3.1, a large normal stress variation in model N7 promotes complex rupture sequences, which is not captured in the W/L_∞ ratio.

In addition, we evaluate whether the observed complexity stems from a high maximum W/L_∞ ratio or from heterogeneous fault properties. We perform a simulation with a constant high value of W/L_∞ of $\sim$250, comparable to the maximum W/L_∞ value in model N12R4D4, but using homogeneous input parameters (Fig. S4). This homogeneous model generates relatively simple, periodic cycles consisting of a system-size and a partial rupture, whose hypocenter depths are consistently located at the base of the seismogenic zone.

By systematically comparing W/L_∞ ratios using a quantitative metric (the complexity score), we find that the W/L_∞ ratio may not serve as an absolute criterion for predicting the degree of complexity among models with substantially different setups. Previous studies emphasizing the control of W/L_∞ ratio on complexity often utilize simple setups, such as depth-independent stress values (e.g., Cattania, 2019), or perform isolated parameter searches, such as changing the D_{RS} value while fixing other parameters (e.g., Barbot, 2019; Lapusta & Rice, 2003). These approaches offer systematic insights into how W/L_∞ affects rupture behavior under a simple, homogeneous setup. However, in models with pronounced heterogeneity, interaction between different forms of heterogeneity may additionally affect the system's complexity, diminishing the power of the W/L_∞ ratio for predicting the level of complexity across different models. This finding

emphasizes that heterogeneity is driving complexity and can produce system behavior that is not easily inferable.

4.3 The Effect of a Low-Rigidity Fault Zone

We find that the presence of a low-rigidity fault zone does not increase the complexity of the earthquake cycle (e.g., compare models N3D1FZ and N3D1). This finding is in line with the comprehensive parameter search by Nie and Barbot (2022), who concluded that low-rigidity fault zones contribute to complexity only by decreasing the nucleation size. Models with and without such low-rigidity fault zones are indistinguishable when they share a similar W/L_∞ ratio.

The observed insensitivity of rupture behavior to the presence of a low-rigidity fault zone in our models may stem from the limited range of rigidity contrasts we explored. Nie and Barbot (2022), in a systematic study, showed that higher rigidity contrast tends to promote more complex ruptures at a fixed characteristic weakening distance (D_{RS}). Abdelmeguid et al. (2019) noted the emergence of partial ruptures as rigidity contrast increases. These findings suggest that a larger rigidity contrast may increase system complexity, possibly due to a reduction of nucleation size. Moreover, the effect of a low-rigidity fault zone may become increasingly important in models beyond pure elastic off-fault behavior, e.g., those incorporating plasticity or viscoelasticity (e.g., Abdelmeguid & Elbanna, 2022; Erickson et al., 2017; Niu et al., 2024; van Dinther et al., 2014; Zhai et al., 2025; Zhao et al., 2024). However, it remains unclear whether incorporating higher rigidity contrasts or inelastic effects is sufficient to break the observed cycle-invariance.

The absence of complex wave interaction in our quasi-dynamic simulations may inhibit the emergence of complex rupture patterns, as pointed out by Nie and Barbot (2022). Previous fully dynamic models have shown changes in rupture behavior, such as a broader depth range of earthquake hypocenters and increased shear stress heterogeneity within the seismogenic zone, when low-rigidity fault zones are present (Y. Huang & Ampuero, 2011; Y. Huang et al., 2014; Thakur et al., 2020; Thakur & Huang, 2024). In this study, models with (N3D1FZ) and without (N3D1) the low-rigidity fault zone show comparable shear stress distributions 1 hour before and after a system-size earthquake (Figure S5).

4.4 Different Rupture Styles of the Aging Law and the Slip Law

In section 3.4, we observe key differences between models using the aging law (model N3R1D2) and the slip law (model N3R1D2-S). The slip law model tends to produce: (1) quasi-periodic earthquake cycles of shorter duration, consisting of fewer earthquakes per cycle, (2) smaller average static stress drop, and (3) smaller peak slip rates during system-size earthquakes.

The rapid cascade of earthquake sequences with fewer smaller earthquakes in the slip law model is consistent with the highly non-linear nature of the slip law. The slip law shows slower growth of fracture energy during rupture acceleration, allowing instability to develop over a smaller length scale (i.e., smaller critical nucleation size) and facilitating easier rupture propagation across the entire fault (Ampuero & Rubin, 2008). Previous studies have shown that the slip law can accommodate unstable slip regardless of the stiffness of the system (Gu et al., 1984; Ranjith & Rice, 1999), particularly when subjected to stress perturbations (Helmstetter & Shaw, 2009; Perfettini & Ampuero, 2008).

While smaller static stress drops under the slip law are well-documented (Hawthorne & Rubin, 2013; He et al., 2003), peak slip rate comparisons between slip and aging laws have yielded varying conclusions across different models. For example, using the slip law, Perfettini and Ampuero (2008) reported higher peak slip rates under finite stress perturbation, while He et al. (2023) observed the opposite within a weakening zone during

the nucleation process. These discrepancies may arise from differences in model setups, such as the spring-slider system or homogeneous frictional properties, since correlations between kinematic parameters may depend on the local heterogeneity of dynamic parameters (Schliwa et al., 2024; Schmedes et al., 2010; Vyas et al., 2023). To the best of our knowledge, this study presents the first systematic comparison of rupture characteristics for the aging and slip laws under more realistic conditions, incorporating fractal heterogeneity in stress and material properties.

4.5 Transition from Aperiodic to Cycle-Invariant Regimes

We observe that most initial heterogeneities are rapidly wiped out after a few cycles (or a few hundred years), even when all three heterogeneous parameters are combined. Models then leave a so-called spin-up phase (Erickson et al., 2020; Hetland & Hager, 2006) and exhibit repeating slip sequences. Among all models explored in this study (Table S2), only model N12R4D4 sustains prolonged aperiodicity for more than 1000 yr (Fig. 6c). This may imply that when heterogeneities are either statistically unpredictable or composed of multiple uncorrelated components, the system requires more time to evolve toward (quasi-)cyclic slip behavior.

Even for model N12R4D4, the slip sequence eventually evolves toward quasi-periodic behavior if simulations are run sufficiently long (Fig. S7). The transition from aperiodic to quasi-periodic sequences occurs after 1750 yr of simulation time, equivalent to 23 system-size earthquakes. This transition from aperiodic to periodic cycles implies that the initial complexity in the modeled earthquake sequences might represent a prolonged spin-up phase and that it might take tens of cycles to completely eliminate the effect of initial conditions.

The loss of complexity in the later stage of the simulation fundamentally questions the possibility of obtaining aperiodic earthquake sequences in 2D antiplane strain quasi-dynamic models. Previous studies that found non-characteristic (i.e., aperiodic) regimes often analyzed only a few hundred years, or equivalently, several system-size cycles, and it is not clear if the reported complexity persists over much longer time intervals (Cattania, 2019; Ito & Kaneko, 2023; Molina-Ormazabal et al., 2023; Nie & Barbot, 2022).

A more sustainable aperiodic behavior of modeled earthquake sequences may be achieved by explicitly accounting for the rough fault geometry (e.g., Cattania & Segall, 2021; Tal & Gabrieli, 2024), rather than approximating the effects of fault roughness (e.g., by applying spatially variable normal stress), as the topography of the fault surface perpetually introduces heterogeneity in stress to the system (Dunham et al., 2011; Fang & Dunham, 2013; Romanet et al., 2020). Whether complexity can be sustained beyond the timespans reported here in 2D antiplane strain quasi-dynamic simulations, and under what conditions, remains an open question for future research.

After the 1750-year transition to a periodic sequence (consisting of 2 repeating cycles), we observe repeating earthquakes ('repeaters'; Uchida & Bürgmann, 2019), such as the two unlabeled events preceding event 81 and event 88 in Figure 6. These repeaters occur at a depth of 11.36 km with a recurrence interval of 152 yr. The repeaters in this model show a significantly smaller slip ($\sim$0.3 m) than that expected from the creeping velocity at the VS area surrounding the repeater asperity ($\sim$5 m), similar to observations of natural repeaters (e.g., Chen et al., 2007; Nadeau & Johnson, 1998). These results suggest that caution should be exercised when using repeaters to infer local creep rates (Turner et al., 2024).

4.6 The Role of Fractal Heterogeneity in Slow Slip Generation

Within the parameter space explored, only models N7, N3R2D1, and N12R4D4 produce SSEs. In models N3R2D1 and N12R4D4, the emergence of SSEs is attributed to

the presence of a conditionally stable VW patch near the base of the seismogenic zone, which is bounded by adjacent VS regions in the heterogeneous $(a-b)$ profiles version 2 and 4 (Fig. S1). In both profiles, the VW patch is sufficiently large to permit nucleation and the adjacent VS regions are wide enough to arrest rupture propagation. This configuration, conditionally stable patches embedded within VS regions, is commonly adopted to generate SSEs in SEAS-type models (e.g., Wei et al., 2013).

The occurrence of SSEs is sensitive to the spatial distribution of fractal heterogeneities, particularly the size of the VS and VW patches, affecting their stability. For example, although models N3R1D1 and N3R2D1 share similar model parameters, only model N3R2D1 produces SSEs. This difference is likely due to the difference in the size of the VS patch near 12 km depth (0.2 km in N3R1D1 vs. 1 km in N3R2D1; Fig. S1). In model N3R1D1, thinner VS zones are less effective as rupture barriers, while thicker VW patches promote faster slip (Lui & Lapusta, 2016; Wei & Shi, 2021). However, heterogeneous $(a-b)$ profiles alone cannot produce SSEs (e.g., model R4, Fig. S9). Rather, the interplay between multiple heterogeneous parameters adds complexity to the system.

In model N7, SSEs are facilitated by patches of low effective normal stress, typically ranging between 0.1-1 MPa. Such low σ_n regions have been widely recognized as a mechanism for generating slow slip events in SEAS simulations (e.g., Y. Liu & Rice, 2007; Rubin, 2008; Wei et al., 2018). Their presence increases the critical nucleation length, allowing the patch to stay between nucleation and instability (Rubin, 2008).

5 Conclusions

We extensively explore the effects of various types of heterogeneities on generating non-characteristic earthquake cycles with considerable complexity in rupture size and hypocenter depth distributions in 2D quasi-dynamic rate-and-state friction simulations. Using the aging law, we find that a broad spectrum of fault slip, including both system-size and partial ruptures, occurs when multiple fractal heterogeneities in both stress and strength parameters are introduced conjointly. Creeping patches are critical for enabling depth-variable earthquake nucleation throughout the entire seismogenic zone due to elevated stressing rates at their margins. The presence of a low-rigidity fault zone adds little to system complexity compared to models with comparable W/L_∞ ratios but without a fault zone.

While model complexity and maximum W/L_∞ ratio exhibit moderate correlation, different models with similar W/L_∞ ratios show varying degrees of complexity. This result highlights that fault slip complexity can be highly model-dependent. As such, caution should be exercised when using the W/L_∞ ratio as a proxy for system complexity, particularly in heterogeneous models.

The most complex aging law model presented here (model N12R4D4) features system-size earthquakes with a range of hypocentral depths, which are consistently preceded by a cascade of partial ruptures, as well as shallow and deep slow slip events. In addition, this model reproduces other observed characteristics of natural faults, such as repeating earthquakes and aseismic transients preceding small-to-moderate-size earthquakes. However, even this most complex sequence transitions from aperiodic to periodic cycles after thousands of years, implying that the effects of initial conditions in cycle simulations may be more persistent than previously thought.

Finally, we compare earthquake sequences under aging and slip law assumptions. The slip law models produce shorter-duration quasi-periodic earthquake cycles, consisting of fewer earthquakes per cycle, smaller average static stress drops, and lower peak slip rates during system-size earthquakes.

The complex slip sequences analyzed in this study may serve as base models for a range of applications, as they resemble natural seismic and aseismic processes. For example, in the companion paper (Yun et al., 2025a), we use these models as reference slip histories for the M_w 7.1 mainshock fault and investigate its triggering responses when subjected to external stress perturbations from the M_w 5.4 foreshock.

Table 1. Base values for the parameters used in the SEAS models using *Tandem*. z is depth in kilometers.

Symbol	Parameter	Value
a	Rate-and-state parameter, direct effect	Varies (see Fig. 1c)
b	Rate-and-state parameter, evolution effect	0.019
D_{RS}	Characteristic state evolution distance	4 mm
f_0	Reference coefficient of friction	0.6
V_0	Reference slip rate	10^{-6} m/s
V_{init}	Initial slip rate	10^{-9} m/s
V_{pl}	Plate loading rate	10^{-9} m/s
σ_n	Background effective normal stress	50 MPa (see Fig. 1b)
τ^0	Background shear stress	Varies (see Fig. 1b)
ν	Poisson's ratio	0.25
W	Seismogenic zone width*	$\sim$10 km
L_f	Rate-and-state fault length	24 km

* May slightly vary due to fractal heterogeneity (see Section 2.2).

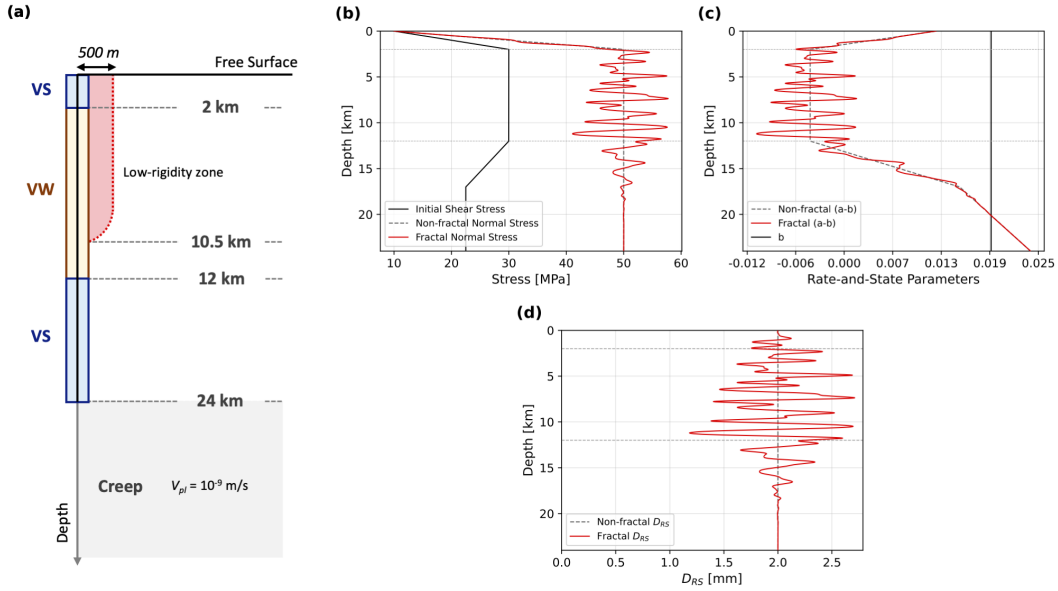

Figure 1. (a) Sketch of the model geometry for the SEAS simulations using *Tandem*. The rate-and-state fault (black vertical line) includes a central velocity-weakening zone (yellow) surrounded by shallow and deep velocity-strengthening zones (blue). The bottom creep zone governed by the constant loading rate (V_{pl}) is shaded in grey. The red-shaded area indicates the spatial extent of a low-rigidity fault zone. As the model represents a perfectly symmetric vertical strike-slip fault, we model only one side of the domain. (b-d) Self-affine fractal distributions of (b) effective normal stress (version 3), (c) rate-and-state parameters (version 1), and (d) characteristic state evolution distance (version 1). The fractal distributions of all three parameters share the same limiting wavelengths of λ_{min} = 500 m and λ_{max} = 2.5 km. See Table S1 for a detailed description of each fractal model.

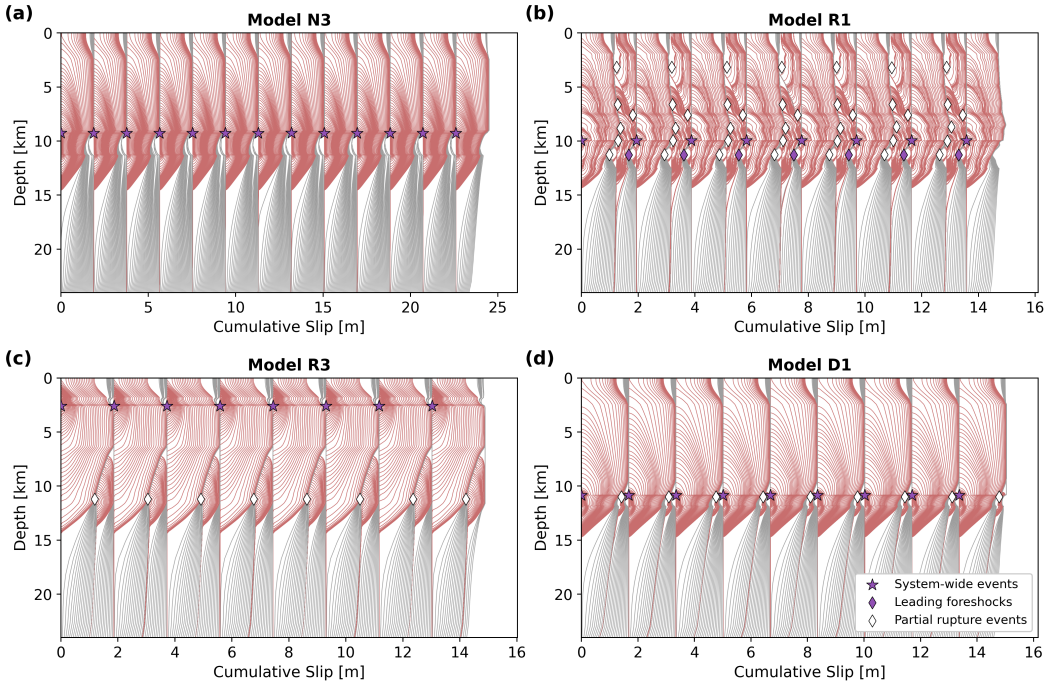

Figure 2. Cumulative slip evolution along the fault in exemplary SEAS simulations with heterogeneity in either stress or strength. (a) Model with heterogeneity in effective normal stress shown in Figure 1b (model N3). (b-c) Models with heterogeneity in $(a - b)$ parameter (b) with (model R1) and (c) without (model R3) the velocity-strengthening patches embedded within the seismogenic layer. Model R1 in panel (b) uses the $(a - b)$ heterogeneity shown in Figure 1c. (d) Model with heterogeneity in D_{RS} parameter shown in Figure 1d (model D1). All models show the cumulative slip omitting the first 200 yr of spin-up time. Pink contours, drawn every 0.5 s, show the coseismic evolution of slip, while grey contours, plotted every 2 yr, show the longer-term evolution of slip. Purple stars, purple diamonds, and white diamonds indicate the hypocenter locations of system-size earthquakes, leading foreshocks, and partial rupture events, respectively.

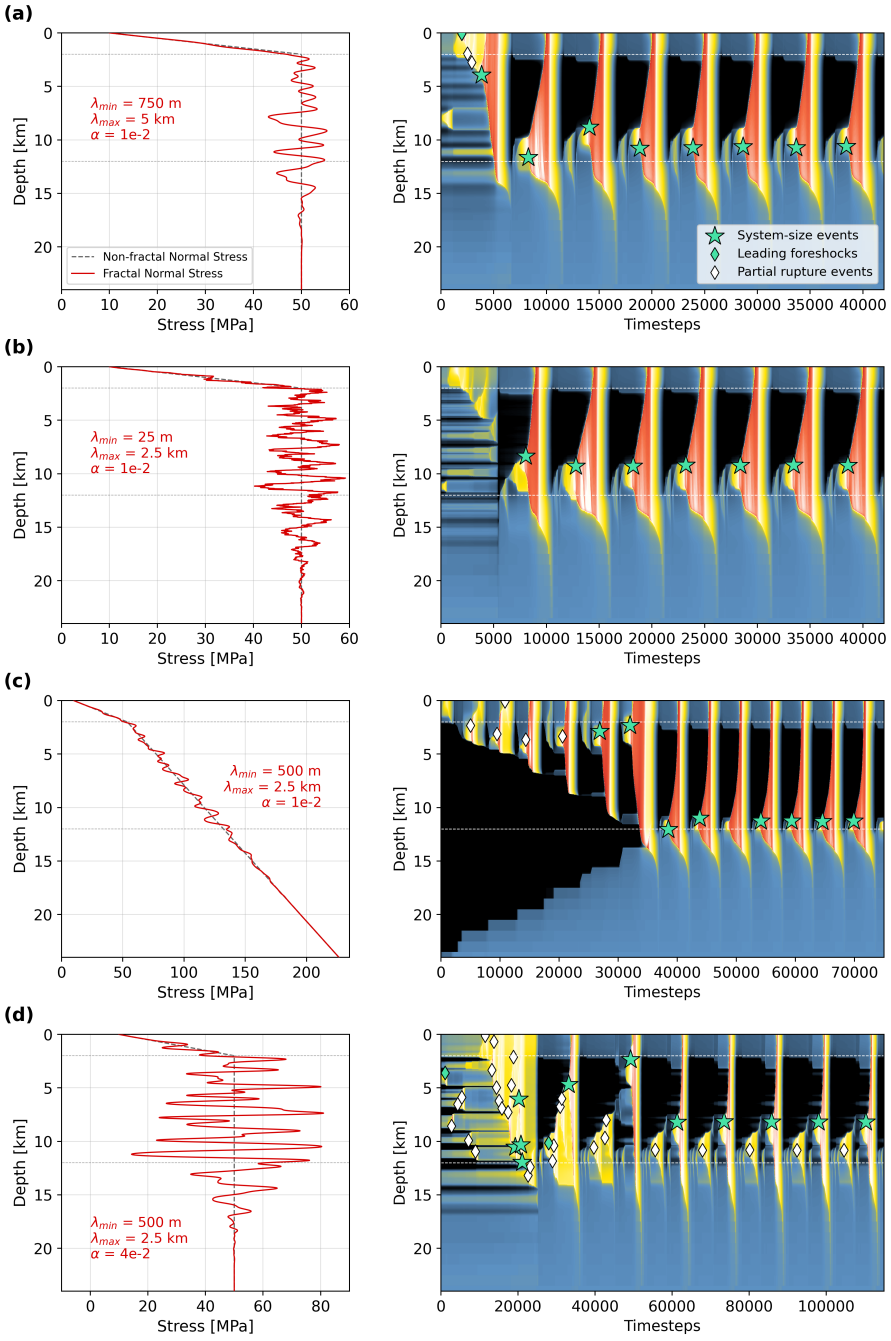

Figure 3. Comparison of SEAS models with heterogeneity only in effective normal stress (group N): models (a) N1 ($\alpha = 10^{-2}$, $\lambda_{min} = 750$ m, $\lambda_{max} = 5$ km), (b) N4 ($\alpha = 10^{-2}$, $\lambda_{min} = 25$ m, $\lambda_{max} = 2.5$ km), (c) Nd1 (depth-dependent; $\alpha = 10^{-2}$, $\lambda_{min} = 500$ m, $\lambda_{max} = 2.5$ km), and (d) N7 ($\alpha = 4 \times 10^{-2}$, $\lambda_{min} = 500$ m, $\lambda_{max} = 2.5$ km). The left column shows the spatial distribution of the normal stress heterogeneity, and the right column shows the resultant spatiotemporal evolution of slip rate. Green stars, green diamonds, and white diamonds indicate the hypocenter locations of system-size earthquakes, leading foreshocks, and partial rupture events, respectively. Numbers next to the markers indicate the event number. α: amplitude-to-wavelength ratio; λ_{min} & λ_{max}: minimum and maximum wavelengths of the fractal variation.

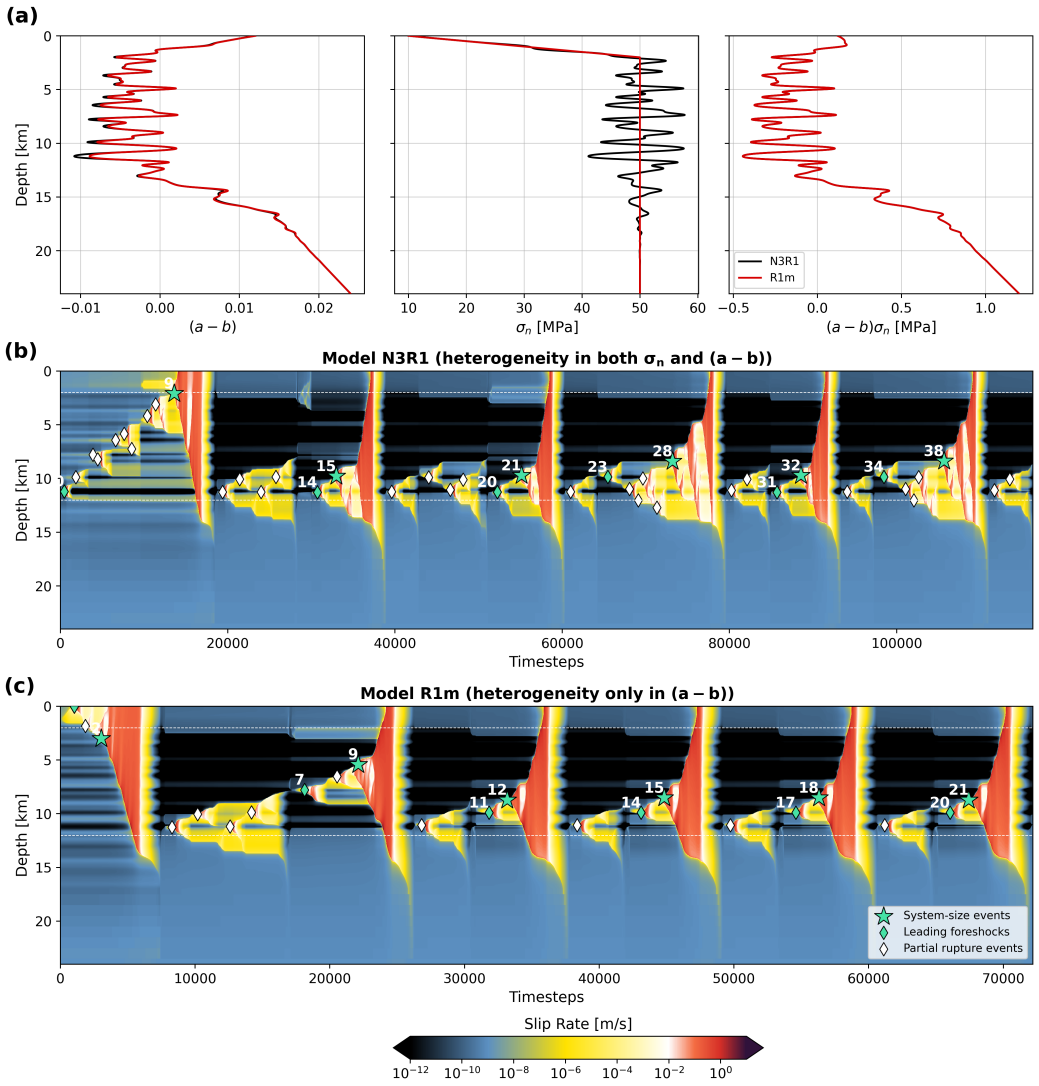

Figure 4. Comparison of model N3R1 and model R1m. (a) Spatial distribution of $(a-b)$, σ_n, and the resultant frictional strength $\sigma_n(a-b)$ used in models N3R1 (black) and R1m (red). (b-c) Spatiotemporal evolution of slip rate during 700-year simulations of (b) model N3R1 and (c) model R1m, showing less complex slip evolution in model R1m. Green stars, green diamonds, and white diamonds indicate the hypocenter locations of system-size earthquakes, leading foreshocks, and partial rupture events, respectively. Numbers next to the markers indicate the event number.

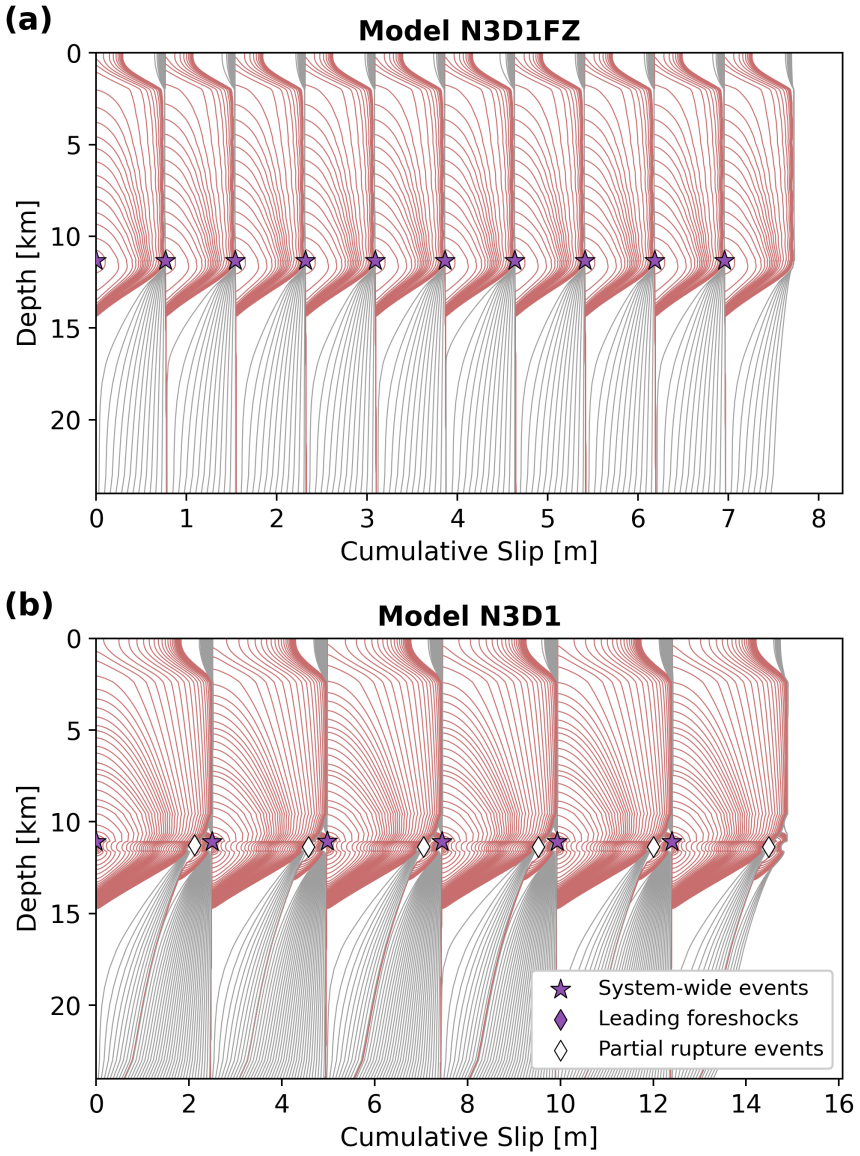

Figure 5. Comparison of SEAS models (a) with and (b) without a low-rigidity fault zone surrounding the fault (red shaded area in Fig. 1a). (a) Model N3D1FZ, featuring a low-rigidity fault zone ($\mu_{FZ} = 20$ GPa) embedded in the bulk with $\mu = 32$ GPa. (b) Model N3D1, featuring a uniformly low $\mu = 20$ GPa in the entire bulk. Both models share fractal heterogeneities in the effective normal stress and characteristic state evolution distance shown in Figures 1b and 1d. All models show the cumulative slip, omitting the first 200 yr of spin-up time. Pink contours, drawn every 0.5 s, show the coseismic evolution of slip, while grey contours, plotted every 2 yr, show the longer-term evolution of slip. Purple stars, purple diamonds, and white diamonds indicate the hypocenter locations of system-size earthquakes, leading foreshocks, and partial rupture events, respectively.

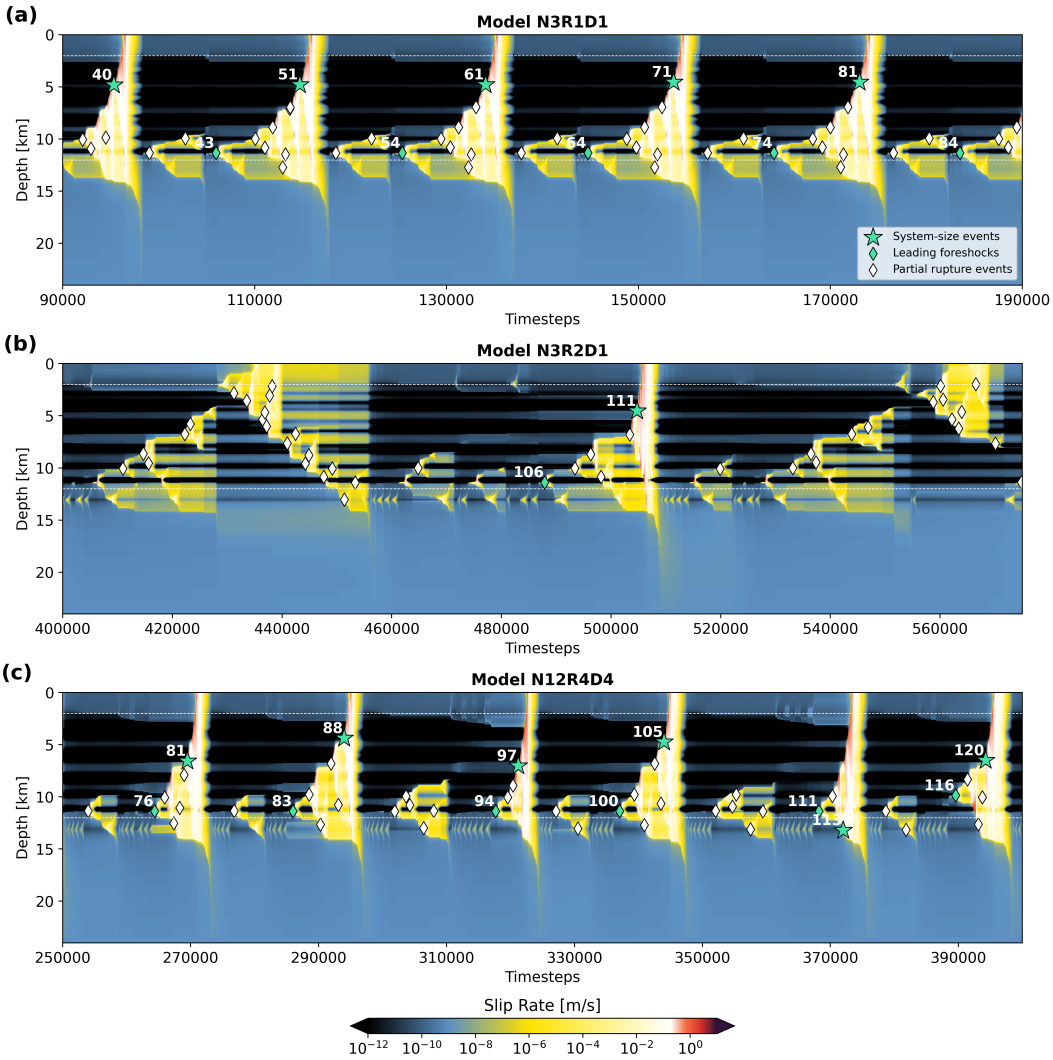

Figure 6. Spatiotemporal evolution of slip rate of SEAS models with heterogeneity in all three parameters (see Section 3.2). The slip rate evolution of (a) model N3R1D1 between 348 yr and 679 yr of simulation time, (b) model N3R2D1 between 387 yr and 537 yr of simulation time, and (c) model N12R4D4 between 745 yr and 1180 yr of simulation time. Green stars, green diamonds, and white diamonds indicate the hypocenter locations of system-size earthquakes, leading foreshocks, and partial rupture events, respectively. Numbers next to the markers indicate the event number.

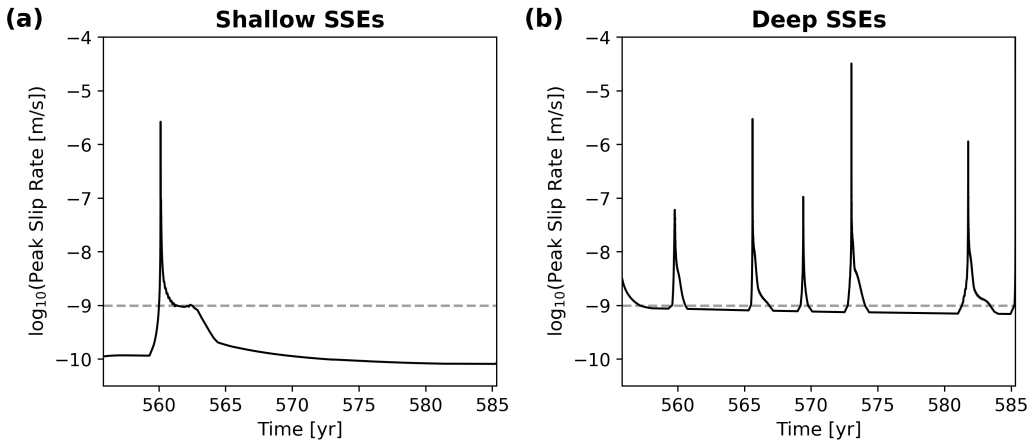

Figure 7. Slow slip events (SSEs) observed in model N3R2D1. (a-b) Peak slip rates of the shallow (<5 km) and the deep (10 km - 20 km) SSEs. Grey dashed lines mark the constant plate loading rate (V_{pl}).

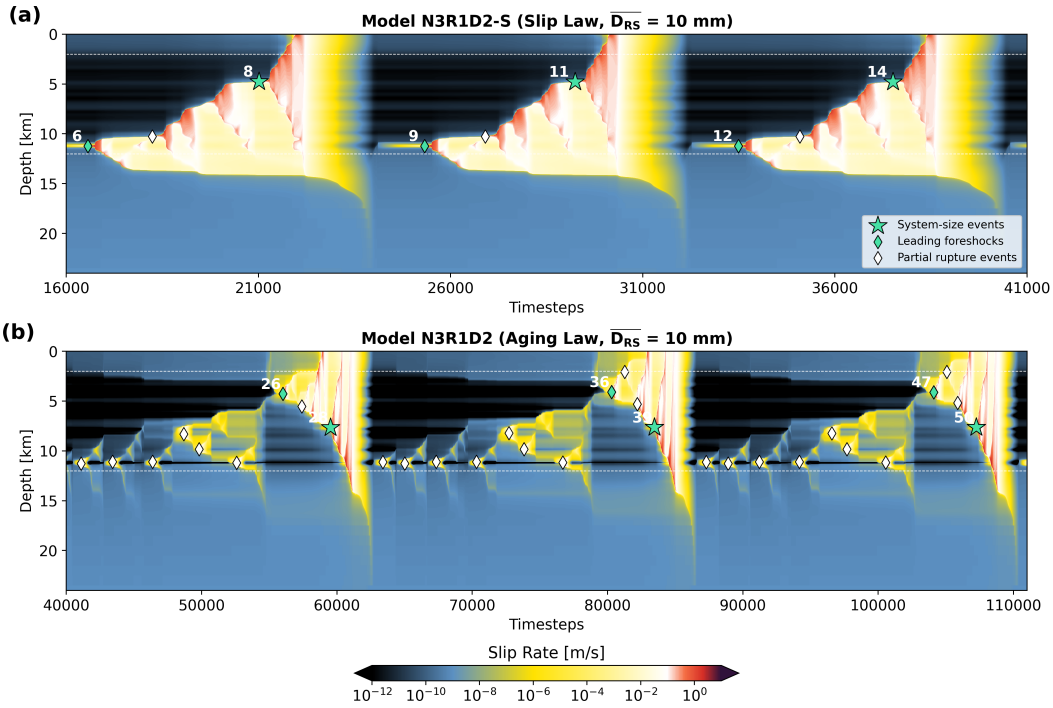

Figure 8. Comparison of spatiotemporal evolution of slip rate of models using (a) slip law (model N3R1D2-S) between 131 yr and 291 yr of simulation time and (b) aging law (model N3R1D2) sharing the same input parameters (see Section 3.4), between 262 yr and 613 yr of simulation time. Green stars, green diamonds, and white diamonds indicate the hypocenter locations of system-size earthquakes, leading foreshocks, and partial rupture events, respectively. Numbers next to the markers indicate the event number.

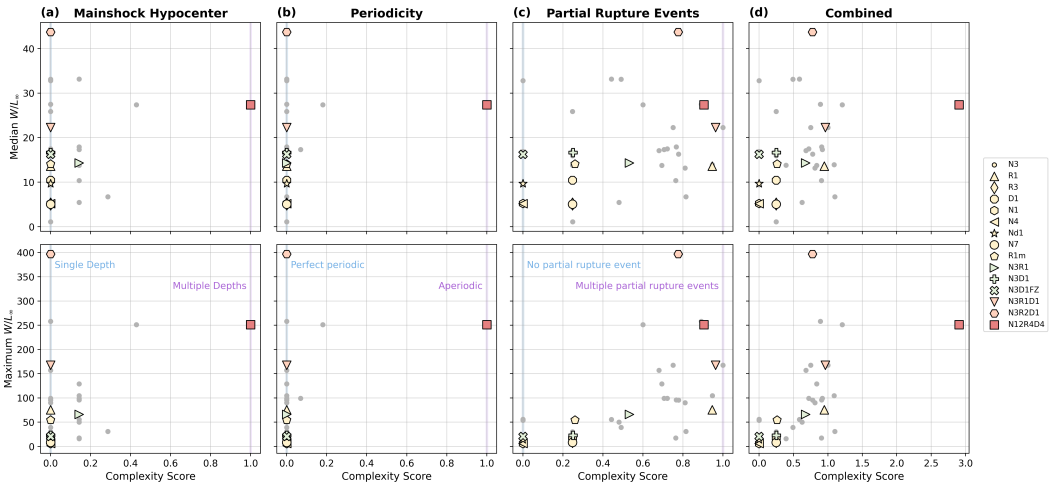

Figure 9. Correlation between the complexity score (Section 2.4) and W/L_∞ ratio for all aging law models (grey dots). The top and bottom rows show the median and maximum W/L_∞ ratios, respectively. (a-c) Individual complexity scores for (a) hypocenter depth heterogeneity of system-size earthquakes, (b) periodicity, and (c) heterogeneity in partial rupture events. (d) Combined complexity score, the sum of the three individual complexity scores, ranging from 0 to 3. Models presented in Figures 2 through 8 are plotted in colors and symbols, as shown in the legend. We colored single heterogeneity models in yellow, double heterogeneity models in light green, and triple heterogeneity models in light pink. The most complex model (N12R4D4) is colored in a dark pink color. See Table S2 for model name definition.

6 Open Research

All input data required for reproducing all models are made available (Yun et al., 2025b). All simulations were conducted using the open-source software *Tandem* (Uphoff et al., 2022). An online documentation is available at `https://tandem.readthedocs.io/en/latest/`. We use dmay/seas-checkpoint branch (commit #1dc36db) for aging law simulations and jyun/state-law branch (commit #5d5c63f) for slip law simulations.

Acknowledgments

We thank Editor Rachel Abercrombie, the Associate Editor, Reviewer Mohamed Abdelmeguid, and the anonymous reviewer for their positive evaluation and constructive comments. We thank Prithvi Thakur, Camilla Cattania, and Junle Jiang for sharing their SEAS codes. We appreciate fruitful discussions with Eric Dunham. YF acknowledges support from NSF (EAR-1841273) and NASA (80NSSC22K0506). AAG and DAM acknowledge support from NSF, grants EAR-2121568 (MTMOD) and OAC-2311208 (Quakeworx). AAG acknowledges support from NSF, grants OAC-2139536 (LCCF-CSA) and EAR-2225286 (CRESCENT), the Southern California Earthquake Center (SCEC awards 24103, 24127, 22135, 23121, 22162), the European Union's Horizon 2020 Research and Innovation Programme (TEAR, grant number 852992), Horizon Europe (ChEESE-2P, grant number 101093038, DT-GEO, grant number 101058129, and Geo-INQUIRE, grant number 101058518), and NASA (80NSSC20K0495). We gratefully acknowledge the computing resources provided by the Institute of Geophysics of LMU Munich (Oeser et al., 2006). We also acknowledge the Gauss Center for Supercomputing e.V. (`https://www.gauss-centre.eu/`) for providing computing time on SuperMUC-NG, hosted at the Leibniz Supercomputing Center (`https://www.lrz.de/`), via project pn49ha.

References

Abdelmeguid, M., & Elbanna, A. (2022). Modeling sequences of earthquakes and aseismic slip (SEAS) in elasto-plastic fault zones with a hybrid finite element spectral boundary integral scheme. *Journal of Geophysical Research: Solid Earth*, *127*(12), e2022JB024548.

Abdelmeguid, M., Ma, X., & Elbanna, A. (2019). A novel hybrid finite element-spectral boundary integral scheme for modeling earthquake cycles: Application to rate and state faults with low-velocity zones. *Journal of Geophysical Research: Solid Earth*, *124*(12), 12854–12881. doi: 10.1029/2019JB018036

Abdelmeguid, M., Mia, M. S., & Elbanna, A. (2024). On the interplay between distributed bulk plasticity and local fault slip in evolving fault zone complexity. *Geophysical Research Letters*, *51*(14), e2023GL108060.

Abhyankar, S., Brown, J., Constantinescu, E., Ghosh, D., & Smith, B. F. (2014). *PETSc/TS: A modern scalable DAE/ODE solver library* (Preprint No. ANL/MCS-P5061-0114). Argonne National Laboratory.

Ampuero, J.-P., & Rubin, A. M. (2008). Earthquake nucleation on rate and state faults – Aging and slip laws. *Journal of Geophysical Research: Solid Earth*, *113*(B1).

Andrews, D., & Barall, M. (2011). Specifying initial stress for dynamic heterogeneous earthquake source models. *Bulletin of the Seismological Society of America*, *101*(5), 2408–2417.

Balay, S., Abhyankar, S., Adams, M. F., Brown, J., Brune, P., Buschelman, K., ... Zhang, H. (2019). *PETSc users manual* (Tech. Rep. No. ANL-95/11 - Revision 3.11). Argonne National Laboratory.

Balay, S., Gropp, W. D., McInnes, L. C., & Smith, B. F. (1997). Efficient management of parallelism in object oriented numerical software libraries. In E. Arge, A. M. Bruaset, & H. P. Langtangen (Eds.), *Modern software tools in scientific computing* (pp. 163–202). Birkhäuser Press.

Barbot, S. (2019). Slow-slip, slow earthquakes, period-two cycles, full and partial ruptures, and deterministic chaos in a single asperity fault. *Tectonophysics*, *768*, 228171.

Barbot, S., Fialko, Y., & Bock, Y. (2009). Postseismic deformation due to the Mw 6.0 2004 Parkfield earthquake: Stress-driven creep on a fault with spatially variable rate-and-state friction parameters. *Journal of Geophysical Research: Solid Earth*, *114*, B07405.

Barbot, S., Lapusta, N., & Avouac, J.-P. (2012). Under the hood of the earthquake machine: Toward predictive modeling of the seismic cycle. *Science*, *336*(6082), 707–710.

Bayart, E., Rubin, A. M., & Marone, C. (2006). Evolution of fault friction following large velocity jumps. In *Agu fall meeting abstracts* (Vol. 2006, pp. S31A–0180).

Beall, A., van den Ende, M., Ampuero, J.-P., Capitanio, F. A., & Fagereng, Å. (2022). Linking earthquake magnitude-frequency statistics and stress in visco-frictional fault zone models. *Geophysical Research Letters*, *49*(20), e2022GL099247.

Beeler, N., Tullis, T., & Weeks, J. (1994). The roles of time and displacement in the evolution effect in rock friction. *Geophysical research letters*, *21*(18), 1987–1990.

Ben-Zion, Y., & Rice, J. R. (1995). Slip patterns and earthquake populations along different classes of faults in elastic solids. *Journal of Geophysical Research: Solid Earth*, *100*(B7), 12959–12983.

Candela, T., Renard, F., Klinger, Y., Mair, K., Schmittbuhl, J., & Brodsky, E. E. (2012). Roughness of fault surfaces over nine decades of length scales. *Journal of Geophysical Research: Solid Earth*, *117*(B8).

Cattania, C. (2019). Complex earthquake sequences on simple faults. *Geophysical Research Letters*, *46*(17-18), 10384–10393.

Cattania, C., & Segall, P. (2019). Crack models of repeating earthquakes predict observed moment-recurrence scaling. *Journal of Geophysical Research: Solid Earth*, *124*(1), 476–503.

Cattania, C., & Segall, P. (2021). Precursory slow slip and foreshocks on rough faults. *Journal of Geophysical Research: Solid Earth*, *126*(4), e2020JB020430.

Chen, K. H., Nadeau, R. M., & Rau, R.-J. (2007). Towards a universal rule on the recurrence interval scaling of repeating earthquakes? *Geophysical Research Letters*, *34*(16).

Chester, F. M., Evans, J. P., & Biegel, R. L. (1993). Internal structure and weakening mechanisms of the San Andreas fault. *Journal of Geophysical Research: Solid Earth*, *98*(B1), 771–786.

Cochard, A., & Madariaga, R. (1996). Complexity of seismicity due to highly rate-dependent friction. *Journal of Geophysical Research: Solid Earth*, *101*(B11), 25321–25336.

Dieterich, J. H. (1979). Modeling of rock friction: 1. Experimental results and constitutive equations. *Journal of Geophysical Research: Solid Earth*, *84*(B5), 2161–2168.

Dieterich, J. H. (1994). A constitutive law for rate of earthquake production and its application to earthquake clustering. *Journal of Geophysical Research: Solid Earth*, *99*(B2), 2601–2618.

Dieterich, J. H., & Kilgore. (1994). Direct observation of frictional contacts: New insights for state-dependent properties. *Pure and applied geophysics*, *143*, 283–302.

Dublanchet, P., Bernard, P., & Favreau, P. (2013). Creep modulation of Omori law generated by a Coulomb stress perturbation in a 3-D rate-and-state asperity model. *Journal of Geophysical Research: Solid Earth*, *118*(9), 4774–4793.

Dunham, E. M., Belanger, D., Cong, L., & Kozdon, J. E. (2011). Earthquake

ruptures with strongly rate-weakening friction and off-fault plasticity, part 2: Nonplanar faults. *Bulletin of the Seismological Society of America*, *101*(5), 2308–2322.

Erickson, B. A., Birnir, B., & Lavallée, D. (2011). Periodicity, chaos and localization in a Burridge–Knopoff model of an earthquake with rate-and-state friction. *Geophysical Journal International*, *187*(1), 178–198.

Erickson, B. A., & Dunham, E. M. (2014). An efficient numerical method for earthquake cycles in heterogeneous media: Alternating subbasin and surface-rupturing events on faults crossing a sedimentary basin. *Journal of Geophysical Research: Solid Earth*, *119*(4), 3290–3316.

Erickson, B. A., Dunham, E. M., & Khosravifar, A. (2017). A finite difference method for off-fault plasticity throughout the earthquake cycle. *Journal of the Mechanics and Physics of Solids*, *109*, 50–77.

Erickson, B. A., Jiang, J., Barall, M., Lapusta, N., Dunham, E. M., Harris, R., ... others (2020). The community code verification exercise for simulating sequences of earthquakes and aseismic slip (SEAS). *Seismological Research Letters*, *91*(2A), 874–890.

Erickson, B. A., Jiang, J., Lambert, V., Barbot, S. D., Abdelmeguid, M., Almquist, M., ... others (2023). Incorporating full elastodynamic effects and dipping fault geometries in community code verification exercises for simulations of earthquake sequences and aseismic slip (SEAS). *Bulletin of the Seismological Society of America*, *113*(2), 499–523.

Fang, Z., & Dunham, E. M. (2013). Additional shear resistance from fault roughness and stress levels on geometrically complex faults. *Journal of Geophysical Research: Solid Earth*, *118*(7), 3642–3654.

Fialko, Y., Sandwell, D., Agnew, D., Simons, M., Shearer, P., & Minster, B. (2002). Deformation on nearby faults induced by the 1999 Hector Mine earthquake. *Science*, *297*, 1858–1862.

Gabriel, A.-A., Garagash, D. I., Palgunadi, K. H., & Mai, P. (2024). Fault size–dependent fracture energy explains multiscale seismicity and cascading earthquakes. *Science*, *385*(6707), eadj9587.

Galvez, P., Somerville, P., Petukhin, A., Ampuero, J.-P., & Peter, D. (2020). Earthquake cycle modelling of multi-segmented faults: dynamic rupture and ground motion simulation of the 1992 M_w 7.3 Landers earthquake. *Pure and Applied Geophysics*, *177*, 2163–2179.

Gu, J.-C., Rice, J. R., Ruina, A., & Tse, S. T. (1984). Slip motion and stability of a single degree of freedom elastic system with rate and state dependent friction. *Journal of the Mechanics and Physics of Solids*, *32*(3), 167–196.

Hawthorne, J. C., & Rubin, A. M. (2013). Laterally propagating slow slip events in a rate and state friction model with a velocity-weakening to velocity-strengthening transition. *Journal of Geophysical Research: Solid Earth*, *118*(7), 3785–3808.

He, C., Wong, T.-f., & Beeler, N. (2003). Scaling of stress drop with recurrence interval and loading velocity for laboratory-derived fault strength relations. *Journal of Geophysical Research: Solid Earth*, *108*(B1).

He, C., Zhang, L., Liu, P., & Chen, Q.-F. (2023). Characterizing the final stage of simulated earthquake nucleation governed by rate-and-state fault friction. *Journal of Geophysical Research: Solid Earth*, *128*(5), e2023JB026422.

Helmstetter, A., & Shaw, B. E. (2009). Afterslip and aftershocks in the rate-and-state friction law. *Journal of geophysical Research: Solid earth*, *114*(B1).

Herrendörfer, R., Van Dinther, Y., Gerya, T., & Dalguer, L. A. (2015). Earthquake supercycle in subduction zones controlled by the width of the seismogenic zone. *Nature Geoscience*, *8*(6), 471–474.

Hetland, E., & Hager, B. (2006). Interseismic strain accumulation: Spin-up, cycle invariance, and irregular rupture sequences. *Geochemistry, Geophysics, Geosys-*

tems, *7*(5).

Hillers, G., Ben-Zion, Y., & Mai, P. (2006). Seismicity on a fault controlled by rate- and state-dependent friction with spatial variations of the critical slip distance. *Journal of Geophysical Research: Solid Earth*, *111*(B1).

Hillers, G., Mai, P., Ben-Zion, Y., & Ampuero, J.-P. (2007). Statistical properties of seismicity of fault zones at different evolutionary stages. *Geophysical Journal International*, *169*(2), 515–533.

Huang, J., & Turcotte, D. L. (1990). Are earthquakes an example of deterministic chaos? *Geophysical Research Letters*, *17*(3), 223–226.

Huang, L., Schwartz, S., & Brodsky, E. (2024). Microseismicity at the Time of a Large Creep Event on the Calaveras Fault is Unresponsive to Stress Changes. *Seismica*, *3*(2).

Huang, Y., & Ampuero, J.-P. (2011). Pulse-like ruptures induced by low-velocity fault zones. *Journal of Geophysical Research: Solid Earth*, *116*(B12).

Huang, Y., Ampuero, J.-P., & Helmberger, D. V. (2014). Earthquake ruptures modulated by waves in damaged fault zones. *Journal of Geophysical Research: Solid Earth*, *119*(4), 3133–3154.

Idini, B., & Ampuero, J.-P. (2020). Fault-zone damage promotes pulse-like rupture and back-propagating fronts via quasi-static effects. *Geophysical Research Letters*, *47*(23), e2020GL090736.

Ito, R., & Kaneko, Y. (2023). Physical mechanism for a temporal decrease of the Gutenberg-Richter b-value prior to a large earthquake. *Journal of Geophysical Research: Solid Earth*, *128*(12), e2023JB027413.

Jiang, J., & Fialko, Y. (2016). Reconciling seismicity and geodetic locking depths on the anza section of the san jacinto fault. *Geophysical Research Letters*, *43*(20), 10–663.

Jiang, J., & Lapusta, N. (2016). Deeper penetration of large earthquakes on seismically quiescent faults. *Science*, *352*(6291), 1293–1297.

Jin, Z., & Fialko, Y. (2020). Finite slip models of the 2019 Ridgecrest earthquake sequence constrained by space geodetic data and aftershock locations. *Bulletin of the Seismological Society of America*, *110*(4), 1660–1679.

Kaneko, Y., Avouac, J.-P., & Lapusta, N. (2010). Towards inferring earthquake patterns from geodetic observations of interseismic coupling. *Nature Geoscience*, *3*(5), 363–369.

Kaneko, Y., Fialko, Y., Sandwell, D., Tong, X., & Furuya, M. (2013). Interseismic deformation and creep along the central section of the North Anatolian Fault (Turkey): InSAR observations and implications for rate-and-state friction properties. *Journal of Geophysical Research: Solid Earth*, *118*(1), 316–331.

Kato, N. (2020). Complexity in the earthquake cycle increases with the number of interacting patches. *Pure and Applied Geophysics*, *177*(10), 4657–4676.

Kato, N., & Tullis, T. E. (2001). A composite rate-and state-dependent law for rock friction. *Geophysical research letters*, *28*(6), 1103–1106.

Kroll, K. A., Dieterich, J. H., Richards-Dinger, K. B., & Oglesby, D. D. (2023). 3-D Simulations of earthquakes rupture jumps: 1. Homogeneous pre-stress conditions. *Geophysical Journal International*, *234*(1), 395–403.

Lambert, V., & Lapusta, N. (2021). Resolving simulated sequences of earthquakes and fault interactions: Implications for physics-based seismic hazard assessment. *Journal of Geophysical Research: Solid Earth*, *126*(10), e2021JB022193.

Lapusta, N., & Liu, Y. (2009). Three-dimensional boundary integral modeling of spontaneous earthquake sequences and aseismic slip. *Journal of Geophysical Research: Solid Earth*, *114*(B9).

Lapusta, N., & Rice, J. R. (2003). Nucleation and early seismic propagation of small and large events in a crustal earthquake model. *Journal of Geophysical Research: Solid Earth*, *108*(B4).

Lapusta, N., Rice, J. R., Ben-Zion, Y., & Zheng, G. (2000). Elastodynamic analysis

for slow tectonic loading with spontaneous rupture episodes on faults with rate-and state-dependent friction. *Journal of Geophysical Research: Solid Earth*, *105*(B10), 23765–23789.

Lee, J.-J., & Bruhn, R. L. (1996). Structural anisotropy of normal fault surfaces. *Journal of Structural Geology*, *18*(8), 1043–1059.

Li, M., Niemeijer, A., & van Dinther, Y. (2025). Earthquake nucleation and slip behavior altered by stochastic normal stress heterogeneity. *Journal of Geophysical Research: Solid Earth*, *130*(1), e2024JB029857.

Li, V. C., & Rice, J. R. (1987). Crustal deformation in great California earthquake cycles. *Journal of Geophysical Research: Solid Earth*, *92*, 11533–11551.

Linde, A. T., Suyehiro, K., Miura, S., Sacks, I. S., & Takagi, A. (1988). Episodic aseismic earthquake precursors. *Nature*, *334*(6182), 513–515.

Lindsey, E. O., & Fialko, Y. (2016). Geodetic constraints on frictional properties and earthquake hazard in the Imperial Valley, Southern California. *Journal of Geophysical Research: Solid Earth*, *121*(2), 1097–1113.

Linker, M., & Dieterich, J. H. (1992). Effects of variable normal stress on rock friction: Observations and constitutive equations. *Journal of Geophysical Research: Solid Earth*, *97*(B4), 4923–4940.

Liu, D., Duan, B., & Luo, B. (2020). EQsimu: a 3-D finite element dynamic earthquake simulator for multicycle dynamics of geometrically complex faults governed by rate-and state-dependent friction. *Geophysical Journal International*, *220*(1), 598–609.

Liu, Y., & Rice, J. R. (2007). Spontaneous and triggered aseismic deformation transients in a subduction fault model. *Journal of Geophysical Research: Solid Earth*, *112*(B9).

Lui, S. K., & Lapusta, N. (2016). Repeating microearthquake sequences interact predominantly through postseismic slip. *Nature communications*, *7*(1), 13020.

Luo, Y., & Ampuero, J.-P. (2018). Stability of faults with heterogeneous friction properties and effective normal stress. *Tectonophysics*, *733*, 257–272.

Luo, Y., & Liu, Z. (2019). Slow-slip recurrent pattern changes: Perturbation responding and possible scenarios of precursor toward a megathrust earthquake. *Geochemistry, Geophysics, Geosystems*, *20*(2), 852–871.

Maurer, J. (2024). Statistical distribution of static stress resolved onto geometrically-rough faults. *Seismica*, *3*(2).

Melgar, D., Taymaz, T., Ganas, A., Crowell, B., Öcalan, T., Kahraman, M., ... Altuntaş, C. (2023). Sub-and super-shear ruptures during the 2023 Mw 7.8 and Mw 7.6 earthquake doublet in SE Türkiye. *Seismica*, *2*(3). doi: 10.26443/seismica.v2i3.387

Mia, M. S., Abdelmeguid, M., & Elbanna, A. E. (2023). The spectrum of fault slip in elastoplastic fault zones. *Earth and Planetary Science Letters*, *619*, 118310.

Mitchell, E., Fialko, Y., & Brown, K. (2015). Frictional properties of gabbro at conditions corresponding to slow slip events in subduction zones. *Geochemistry, Geophysics, Geosystems*, *16*(11), 4006–4020.

Mitchell, E., Fialko, Y., & Brown, K. (2016). Velocity-weakening behavior of Westerly granite at temperature up to 600° C. *Journal of Geophysical Research: Solid Earth*, *121*, 6932–6946.

Molina-Ormazabal, D., Ampuero, J.-P., & Tassara, A. (2023). Diverse slip behaviour of velocity-weakening fault barriers. *Nature Geoscience*, *16*(12), 1200–1207.

Nadeau, R. M., & Johnson, L. R. (1998). Seismological studies at Parkfield VI: Moment release rates and estimates of source parameters for small repeating earthquakes. *Bulletin of the Seismological Society of America*, *88*(3), 790–814.

Nagata, K., Nakatani, M., & Yoshida, S. (2012). A revised rate-and state-dependent friction law obtained by constraining constitutive and evolution laws separately with laboratory data. *Journal of Geophysical Research: Solid Earth*, *117*(B2).

Nakata, R., Ando, R., Hori, T., & Ide, S. (2011). Generation mechanism of slow

earthquakes: Numerical analysis based on a dynamic model with brittle-ductile mixed fault heterogeneity. *Journal of Geophysical Research: Solid Earth*, *116*(B8).

Nie, S., & Barbot, S. (2022). Rupture styles linked to recurrence patterns in seismic cycles with a compliant fault zone. *Earth and Planetary Science Letters*, *591*, 117593.

Niu, Z., Gabriel, A.-A., Seelinger, L., & Igel, H. (2024). Modeling and quantifying parameter uncertainty of co-seismic non-classical nonlinearity in rocks. *Journal of Geophysical Research: Solid Earth*, *129*(1), e2023JB027149.

Oeser, J., Bunge, H.-P., & Mohr, M. (2006). Cluster design in the earth sciences tethys. In *International conference on high performance computing and communications* (pp. 31–40).

Ozawa, S., & Ando, R. (2021). Mainshock and aftershock sequence simulation in geometrically complex fault zones. *Journal of Geophysical Research: Solid Earth*, *126*(2), e2020JB020865.

Ozawa, S., Yang, Y., & Dunham, E. M. (2024). Fault-valve instability: A mechanism for slow slip events. *Journal of Geophysical Research: Solid Earth*, *129*(10), e2024JB029165.

Perez-Silva, A., Kaneko, Y., Savage, M., Wallace, L., Li, D., & Williams, C. (2022). Segmentation of Shallow Slow Slip Events at the Hikurangi Subduction Zone Explained by Along-Strike Changes in Fault Geometry and Plate Convergence Rates. *Journal of Geophysical Research: Solid Earth*, *127*(1), e2021JB022913.

Perfettini, H., & Ampuero, J.-P. (2008). Dynamics of a velocity strengthening fault region: Implications for slow earthquakes and postseismic slip. *Journal of Geophysical Research: Solid Earth*, *113*(B9).

Perfettini, H., & Avouac, J.-P. (2007). Modeling afterslip and aftershocks following the 1992 Landers earthquake. *Journal of Geophysical Research: Solid Earth*, *112*.

Perfettini, H., Schmittbuhl, J., & Cochard, A. (2003a). Shear and normal load perturbations on a two-dimensional continuous fault: 1. Static triggering. *Journal of Geophysical Research: Solid Earth*, *108*(B9).

Perfettini, H., Schmittbuhl, J., & Cochard, A. (2003b). Shear and normal load perturbations on a two-dimensional continuous fault: 2. Dynamic triggering. *Journal of Geophysical Research: Solid Earth*, *108*(B9).

Pignalberi, F., Giorgetti, C., Noël, C., Marone, C., Collettini, C., & Scuderi, M. M. (2024). The effect of normal stress oscillations on fault slip behavior near the stability transition from stable to unstable motion. *Journal of Geophysical Research: Solid Earth*, *129*(2), e2023JB027470.

Pranger, C. C. (2020). *Unstable physical processes operating on self-governing fault systems, improved modeling methodology* (Unpublished doctoral dissertation). ETH Zurich.

Ranjith, K., & Rice, J. R. (1999). Stability of quasi-static slip in a single degree of freedom elastic system with rate and state dependent friction. *Journal of the Mechanics and Physics of Solids*, *47*(6), 1207–1218.

Renard, F., & Candela, T. (2017). Scaling of fault roughness and implications for earthquake mechanics. *Fault zone dynamic processes: Evolution of fault properties during seismic rupture*, 195–215.

Renard, F., Voisin, C., Marsan, D., & Schmittbuhl, J. (2006). High resolution 3D laser scanner measurements of a strike-slip fault quantify its morphological anisotropy at all scales. *Geophysical Research Letters*, *33*(4).

Rice, J. R. (1993). Spatio-temporal complexity of slip on a fault. *Journal of Geophysical Research: Solid Earth*, *98*(B6), 9885–9907.

Rice, J. R., & Ben-Zion, Y. (1996). Slip complexity in earthquake fault models. *Proceedings of the National Academy of Sciences*, *93*(9), 3811–3818.

Romanet, P., Sato, D. S., & Ando, R. (2020). Curvature, a mechanical link between

the geometrical complexities of a fault: Application to bends, kinks and rough faults. *Geophysical Journal International*, *223*(1), 211–232.

Ross, Z. E., Cochran, E. S., Trugman, D. T., & Smith, J. D. (2020). 3D fault architecture controls the dynamism of earthquake swarms. *Science*, *368*(6497), 1357–1361.

Rousset, B., Bürgmann, R., & Campillo, M. (2019). Slow slip events in the roots of the San Andreas fault. *Science advances*, *5*(2), eaav3274.

Rubin, A. M. (2008). Episodic slow slip events and rate-and-state friction. *Journal of Geophysical Research: Solid Earth*, *113*(B11).

Rubin, A. M., & Ampuero, J.-P. (2005). Earthquake nucleation on (aging) rate and state faults. *Journal of Geophysical Research: Solid Earth*, *110*(B11).

Ruina, A. (1983). Slip instability and state variable friction laws. *Journal of Geophysical Research: Solid Earth*, *88*(B12), 10359–10370.

Sato, D. S., Nakatani, M., & Ando, R. (2025). Reconciling aging and slip state evolutions from laboratory-derived canons of rate-and-state friction. *Geophysical Journal International*, *240*(3), 1855–1899.

Schliwa, N., Gabriel, A.-A., Premus, J., & Gallovič, F. (2024). The linked complexity of coseismic and postseismic faulting revealed by seismo-geodetic dynamic inversion of the 2004 Parkfield earthquake. *Journal of Geophysical Research: Solid Earth*, *129*(12), e2024JB029410.

Schmedes, J., Archuleta, R. J., & Lavallée, D. (2010). Correlation of earthquake source parameters inferred from dynamic rupture simulations. *Journal of Geophysical Research: Solid Earth*, *115*(B3).

Shaw, B. E., & Rice, J. R. (2000). Existence of continuum complexity in the elastodynamics of repeated fault ruptures. *Journal of Geophysical Research: Solid Earth*, *105*(B10), 23791–23810.

Shi, Z., & Day, S. M. (2013). Rupture dynamics and ground motion from 3-D rough-fault simulations. *Journal of Geophysical Research: Solid Earth*, *118*(3), 1122–1141.

Tal, Y., & Gabrieli, T. (2024). Dual effect of roughness during earthquake rupture sequences on faults with strongly rate-weakening friction. *Earth and Planetary Science Letters*, *637*, 118738.

Tal, Y., Hager, B. H., & Ampuero, J. P. (2018). The effects of fault roughness on the earthquake nucleation process. *Journal of Geophysical Research: Solid Earth*, *123*(1), 437–456.

Taufiqurrahman, T., Gabriel, A.-A., Li, D., Ulrich, T., Li, B., Carena, S., ... Gallovič, F. (2023). Dynamics, interactions and delays of the 2019 Ridgecrest rupture sequence. *Nature*, *618*(7964), 308–315.

Thakur, P., & Huang, Y. (2024). The effects of precursory velocity changes on earthquake nucleation and stress evolution in dynamic earthquake cycle simulations. *Earth and Planetary Science Letters*, *637*, 118727.

Thakur, P., Huang, Y., & Kaneko, Y. (2020). Effects of low-velocity fault damage zones on long-term earthquake behaviors on mature strike-slip faults. *Journal of Geophysical Research: Solid Earth*, *125*(8), e2020JB019587.

Thomas, M. Y., Lapusta, N., Noda, H., & Avouac, J.-P. (2014). Quasi-dynamic versus fully dynamic simulations of earthquakes and aseismic slip with and without enhanced coseismic weakening. *Journal of Geophysical Research: Solid Earth*, *119*(3), 1986–2004.

Thurber, C. H. (1996). Creep events preceding small to moderate earthquakes on the San Andreas fault. *Nature*, *380*(6573), 425–428.

Thurber, C. H., & Sessions, R. (1998). Assessment of creep events as potential earthquake precursors: application to the creeping section of the San Andreas fault, California. *pure and applied geophysics*, *152*, 685–705.

Tse, S. T., & Rice, J. R. (1986). Crustal earthquake instability in relation to the depth variation of frictional slip properties. *Journal of Geophysical Research:*

Solid Earth, *91*(B9), 9452–9472.

Turner, A., Hawthorne, J. C., & Cattania, C. (2024). Partial ruptures cannot explain the long recurrence intervals of repeating earthquakes. *Journal of Geophysical Research: Solid Earth*, *129*(1), e2023JB027870.

Uchida, N., & Bürgmann, R. (2019). Repeating earthquakes. *Annual Review of Earth and Planetary Sciences*, *47*(1), 305–332.

Uphoff, C., May, D. A., & Gabriel, A.-A. (2022). *A discontinuous Galerkin method for sequences of earthquakes and aseismic slip on multiple faults using unstructured curvilinear grids. Geophysical Journal International.* (Version 1.0) [Software]. Zenodo. doi: https://doi.org/10.5281/zenodo.5796104

Uphoff, C., May, D. A., & Gabriel, A.-A. (2023). A discontinuous Galerkin method for sequences of earthquakes and aseismic slip on multiple faults using unstructured curvilinear grids. *Geophysical Journal International*, *233*(1), 586–626.

van Dinther, Y., Mai, P. M., Dalguer, L., & Gerya, T. (2014). Modeling the seismic cycle in subduction zones: The role and spatiotemporal occurrence of off-megathrust earthquakes. *Geophysical Research Letters*, *41*(4), 1194–1201.

Vavra, E. J., Fialko, Y., Rockwell, T., Bilham, R., Štěpančíková, P., Stemberk, J., ... Stemberk, J. (2024). Characteristic slow-slip events on the Superstition Hills Fault, Southern California. *Geophysical Research Letters*, *51*(12), e2023GL107244.

Vyas, J. C., Gabriel, A.-A., Ulrich, T., Mai, P., & Ampuero, J.-P. (2023). How does thermal pressurization of pore fluids affect 3D strike-slip earthquake dynamics and ground motions? *Bulletin of the Seismological Society of America*, *113*(5), 1992–2008.

Waldhauser, F., & Schaff, D. P. (2008). Large-scale relocation of two decades of Northern California seismicity using cross-correlation and double-difference methods. *Journal of Geophysical Research: Solid Earth*, *113*(B8).

Wang, K., & Fialko, Y. (2014). Space geodetic observations and models of postseismic deformation due to the 2005 M7.6 Kashmir (Pakistan) earthquake. *Journal of Geophysical Research: Solid Earth*, *119*(9), 7306–7318.

Wang, S. (2024). Toward quantitative characterization of simulated earthquake-cycle complexities. *Scientific Reports*, *14*(1), 16811.

Wei, M., Kaneko, Y., Liu, Y., & McGuire, J. J. (2013). Episodic fault creep events in California controlled by shallow frictional heterogeneity. *Nature geoscience*, *6*(7), 566–570.

Wei, M., Kaneko, Y., Shi, P., & Liu, Y. (2018). Numerical modeling of dynamically triggered shallow slow slip events in New Zealand by the 2016 M_w 7.8 Kaikoura earthquake. *Geophysical Research Letters*, *45*(10), 4764–4772.

Wei, M., Sandwell, D., & Fialko, Y. (2009). A silent M4.8 slip event of October 3-6, 2006, on the Superstition Hills fault, Southern California. *Journal of Geophysical Research: Solid Earth*, B07402.

Wei, M., & Shi, P. (2021). Synchronization of Earthquake Cycles of Adjacent Segments on Oceanic Transform Faults Revealed by Numerical Simulation in the Framework of Rate-and-State Friction. *Journal of Geophysical Research: Solid Earth*, *126*(1), e2020JB020231.

Yin, Y., Galvez, P., Heimisson, E. R., & Wiemer, S. (2023). The role of three-dimensional fault interactions in creating complex seismic sequences. *Earth and Planetary Science Letters*, *606*, 118056.

Yoshida, S., Maeda, T., & Kato, N. (2020). Earthquake triggering model based on normal-stress-dependent Nagata law: application to the 2016 Mie offshore earthquake. *Earth, Planets and Space*, *72*, 1–13.

Yun, J., Gabriel, A.-A., May, D. A., & Fialko, Y. (2025a). Controls of Dynamic and Static Stress Changes and Aseismic Slip on Delayed Earthquake Triggering: Application to the 2019 Ridgecrest Earthquake Sequence. *Journal of Geophysical Research: Solid Earth*.

Yun, J., Gabriel, A.-A., May, D. A., & Fialko, Y. (2025b). *Supplementary material for "Effects of Stress and Friction Heterogeneity on Spatiotemporal Complexity of Seismic and Aseismic Slip on Strike-Slip Faults".* (Version v1) [Dataset]. Zenodo. doi: https://doi.org/10.5281/zenodo.13918003

Zhai, P., Huang, Y., Liang, C., & Ampuero, J.-P. (2025). Fully dynamic seismic cycle simulations in co-evolving fault damage zones controlled by damage rheology. *Geophysical Journal International*, *242*(3), ggaf274.

Zhang, C., Oglesby, D. D., & Xu, G. (2006). Earthquake nucleation on dip-slip faults with depth-dependent frictional properties. *Journal of Geophysical Research: Solid Earth*, *111*(B7).

Zhao, C., Mia, M. S., Elbanna, A., & Ben-Zion, Y. (2024). Dynamic rupture modeling in a complex fault zone with distributed and localized damage. *Mechanics of Materials*, *198*, 105139.

Zhu, W., Allison, K. L., Dunham, E. M., & Yang, Y. (2020). Fault valving and pore pressure evolution in simulations of earthquake sequences and aseismic slip. *Nature communications*, *11*(1), 4833.

Ziv, A., & Cochard, A. (2006). Quasi-dynamic modeling of seismicity on a fault with depth-variable rate-and state-dependent friction. *Journal of Geophysical Research: Solid Earth*, *111*(B8).

Supporting Information for "Effects of Stress and Friction Heterogeneity on Spatiotemporal Complexity of Seismic and Aseismic Slip on Strike-Slip Faults"

Jeena Yun[1], Alice-Agnes Gabriel[1,2], Dave A. May[1], and Yuri Fialko[1]

[1]Scripps Institution of Oceanography, University of California San Diego, La Jolla, CA, USA

[2]Department of Earth and Environmental Sciences, Ludwig-Maximilians Universität München, Munich, Germany

Contents of this file

Text S1. Numerical Resolution of Volumetric Discontinuous Galerkin Seismic Cycle Models with *Tandem*

We analyze the two most important length scales that need to be resolved in seismic cycle models: the process zone size (Λ_0) and the critical nucleation size (L_∞ defined in the main text; Erickson et al., 2020; Jiang et al., 2022; Rice, 1993). The quasi-static process zone is the area near the rupture front where the fault dynamically weakens, which can be estimated as follows (Day et al., 2005):

$$\Lambda_0 = C\frac{\mu D_{RS}}{b\sigma_n}$$

with C being a constant of an order of 1. For the most complex aging law model (model N12R4D4; see Section 3.3), the smallest values of Λ_0 and L_∞ are 25.47 m and 39.83 m, respectively.

Tandem is a volume-based discontinuous Galerkin code (Uphoff et al., 2023) and must discretize the 2D domain with sufficiently small elements to resolve both Λ_0 and L_∞. To ease computation, we use static gradual mesh coarsening, in which high resolution can be localized in a region around the fault. The minimum element size is prescribed at the fault.

The high-order basis function in *Tandem*'s discontinuous Galerkin scheme provides sub-element resolution, allowing larger element sizes compared to low-order methods without sacrificing accuracy (Uphoff et al., 2023). In this study, we use a basis function of polynomial degree 6 and take an on-fault (minimum) element size (Δz) of 25 m, resulting in an effective element size of $\sim$4 m per degree of freedom. This model resolves the minimum length scale with 6 elements. The element sizes gradually increase up to 50 km at boundaries, located 400 km away from the fault.

To verify the effective resolution of the model, we compare this model with a higher resolution model using a smaller Δz of 10 m, resulting in the smallest effective element size of ∼1.6 m. The two models evolve identically until ∼150 yr of simulation time. Afterward, minor deviations gradually accumulate (Fig. S8a). These deviations are likely resulting from accumulated round-off errors over time. Since the problem is highly nonlinear, small round-off errors can lead to a visible deviation between equivalent models (i.e., Erickson et al., 2020). To reach 300 yr of simulation time, the Δz =10 m model takes 3 times more steps than the Δz =25 m model, which potentially allows more round-off error to accrue.

Regardless of the minor difference between the two models, the characteristic complexities in the earthquake cycle (e.g., the cascade of partial ruptures, shallow and deep slow slip events, and a range of hypocenter depths) spontaneously emerge in both models. The qualitative similarity implies that these complexities are not the artifacts observed in inherently discrete models induced by the oversized cells (Erickson et al., 2020; Rice, 1993; Rice & Ben-Zion, 1996).

Slip law simulations require a finer spatial resolution to accurately resolve the nucleation size $L_b = \mu D_{RS}/b\sigma_n$ (Dieterich, 1992), as noted by Ampuero and Rubin (2008) who used grid spacings between $L_b/50 - L_b/150$. In our slip law models (models N3R1D2-S and N12R4D6-S; see Section 3.4), the minimum L_b is ∼120-150 m. We use $\Delta z = L_b/10 \approx$ 10 m, thereby resolving L_b with 70-90 elements.

We here do not perform a mesh dependence analysis for the slip law models due to their high computational cost. Instead, we assess mesh dependence using aging law models with identical input parameters (models N3R1D2 and N12R4D6; see Section 3.4). These models use $\Delta z = 125$ m, resolving the minimum process zone size with ∼6 elements. We

test mesh dependence by rerunning model N12R4D6 using a smaller $\Delta z = 25$ m. Both simulations yield nearly identical results (Fig. S8b), including identical peak slip rate evolution, indicating that the $\Delta z = 125$ m mesh provides sufficient resolution. We note that both meshes for model N12R4D6 require 3-5 times fewer total time steps to reach 300 yr compared to the more complex model N12R4D4.

Text S2. Impact of Post-Processing on Complexity Estimation

To determine the threshold velocity (V_{ths}) for event classification in each model, we test several values and select the one that best aligns earthquake timing and hypocenter locations with the spatiotemporal evolution of slip rate, based on visual inspection. The chosen V_{ths} values range from 0.01 m/s for models with simple slip history to 0.2 m/s for models with more complex slip patterns.

The V_{ths} values for complex models in this study are largely consistent with the $V_{\text{dyn}} = a\sigma_n/\eta$ estimate introduced by Rubin and Ampuero (2005), the velocity above which the radiation damping term (Eq. (2)) starts to be dominant compared to the direct effect in RSF. For most models in this study, V_{dyn} falls between 0.1-0.3 m/s. However, for simple models, we utilize $V_{ths} = 0.01$ m/s to account for the lower peak slip velocities of partial ruptures.

In general, we do not expect the post-processing procedures, including event classification, to affect the key findings of this study. When estimating the complexity score (Section 2.4), we account for possible uncertainties, e.g., by grouping hypocenters within 0.5 km bins when estimating the complexity for hypocenter depth heterogeneity of system-size earthquakes. We normalize the scores to be a relative indicator within the parameter space we explored, without interpreting absolute values of the complexity score.

Text S3. Minimal Impact of Hurst Exponent on Earthquake Cycles

In this study, we explore two Hurst exponent values (H in Eq. (7) in the main text): $H = 0.7$ (self-affine) and $H = 1.9$. A larger Hurst exponent of 1.9 produces fractal profiles that are smoother at shorter length scales than self-affine profiles (Fig. S9). We compare slip patterns for fractal heterogeneity in $(a - b)$ (denoted as group R), D_{RS} (denoted as group D), and σ_n (denoted as group N), using both Hurst exponent values. Overall, changes in characteristics of rupture evolution due to this change in Hurst exponent are minor for groups D and N (Figs. S9b-c). For example, for both H values, repeating cycles consisting of a pair of a partial rupture and a system-size rupture are observed in group D (Fig. S9b), and regular occurrences of system-size ruptures are observed in group N (Fig. S9c). By increasing H from 0.7 to 1.9, the recurrence interval of system-size earthquakes changes by a decade or two, from ∼50 yr to ∼70 yr in group D and from ∼60 yr to ∼50 yr in group N. The complexity score (as defined in Section 2.4 of the main text) is identical for both Hurst exponents in groups N and D.

The effect of different Hurst exponents is more pronounced in group R (Fig. S9a). This likely stems from changes in the widths of VS patches. Enriched small-wavelength variation in the self-affine model (red line in Fig. S9a) reduces the width of VS patches (e.g., at 7 km and 12 km depth). These narrower VS patches allow partial ruptures to propagate further towards shallower depths, promoting additional shallow partial rupture sequences, and resulting in a higher estimated complexity score.

Text S4. Features Specific to Normal Stress Heterogeneity Version 12

As discussed in Section 3.2, we obtain the most complex slip evolution when combining normal stress heterogeneity version 12 with other heterogeneities (model N12R4D4). We

find that including this specific heterogeneity produces features that are not observed in other models using $H = 0.7$.

Comparing model N12R4D4 and N12R4D4-2 illustrates clear control of W/L_∞ on the system's complexity, including its periodicity (i.e., Barbot, 2019; Cattania, 2019). The two models share the same set of parameters, except that model N12R4D4 has a lower bulk rigidity ($\mu = 32$ GPa in N12R4D4-2 vs. $\mu = 20$ GPa in N12R4D4), resulting in a smaller L_∞ and a higher value of W/L_∞. Both models produce complex sequences with a wide range of hypocenter depths and a diverse spectrum of ruptures (Fig. S10). However, model N12R4D4-2 shows a periodic cycle, while model N12R4D4 shows aperiodic sequences with a higher combined complex score (Table S2).

Comparing models N12D4FZ and N12D4 shows that the presence of the low-rigidity fault zone could promote pulse-like propagation of rupture, some with back-propagating rupture fronts (Beroza & Spudich, 1988; Ding et al., 2024; Flores-Cuba et al., 2024; Idini & Ampuero, 2020). The two models share the same fractal heterogeneity, but model N12D4FZ includes a low-rigidity fault zone ($\mu_{FZ} = 20$ GPa & $\mu = 32$ GPa), while model N12D4 has a uniformly low $\mu = 20$ GPa in the entire bulk. Multiple slip pulses are clearly visible in the N12D4FZ model (Figs. S2a-b) in contrast to the N12D4 model, which exhibits crack-like ruptures (Figs. S2c-d). After $\sim$7 s after the start of a system-size earthquake in the N12D4FZ model, one of the slip pulses seems to propagate back towards the hypocenter and re-ruptures the nearly healed part (i.e., $V < 1$ cm/s) of the fault (white-colored area in Fig. S2). Also, model N12D4FZ exhibits reduced peak slip rate and recurrence interval of the system-size earthquakes compared to model N12D4, as

reported by previous studies (Abdelmeguid et al., 2019; Flores-Cuba et al., 2024; Kaneko et al., 2011).

Back-propagating slip pulses spontaneously emerge in the quasi-dynamic model with a low-rigidity fault zone presented in this study. Although back-propagating ruptures have often been associated with dynamic effects such as free-surface reflection (Burridge & Halliday, 1971; Ding et al., 2024; Kaneko & Lapusta, 2010; Huang et al., 2012), seismic wave interference (Ding et al., 2024; Flores-Cuba et al., 2024), or rapid coseismic weakening and healing (Gabriel et al., 2012), they have also been previously observed in quasi-dynamic simulations (e.g., Barbot, 2021; Cattania, 2019; Yingdi & Ampuero, 2017). Idini and Ampuero (2020) explains the existence of such back-propagating fronts in quasi-dynamic simulations by deriving a static stress transfer kernel in relation to the nearest-neighbor model, such as the Burridge-Knopoff model (Burridge & Knopoff, 1967). These analytical results predict the prevalence of slip pulses as the damage level within a low-rigidity fault zone increases. The crack-to-pulse transition leaves slip deficits, which give rise to back-propagating fronts (Flores-Cuba et al., 2024).

The back-propagating slip pulses are not exclusive to highly complex models. For example, the N12D4FZ model shows cycle-invariant rupture characteristics with a single earthquake per cycle (combined complexity score of 0.2), indicating that such pulses can arise in relatively simple setups. However, we note that the back-propagating slip pulses are only observed under this specific set of heterogeneities.

References

Abdelmeguid, M., Ma, X., & Elbanna, A. (2019). A novel hybrid finite element-spectral boundary integral scheme for modeling earthquake cycles: Application to rate and

state faults with low-velocity zones. *Journal of Geophysical Research: Solid Earth*, *124*(12), 12854–12881. doi: 10.1029/2019JB018036

Ampuero, J.-P., & Rubin, A. M. (2008). Earthquake nucleation on rate and state faults – Aging and slip laws. *Journal of Geophysical Research: Solid Earth*, *113*(B1).

Barbot, S. (2019). Slow-slip, slow earthquakes, period-two cycles, full and partial ruptures, and deterministic chaos in a single asperity fault. *Tectonophysics*, *768*, 228171.

Barbot, S. (2021). A spectral boundary-integral method for quasi-dynamic ruptures of multiple parallel faults. *Bulletin of the Seismological Society of America*, *111*(3), 1614–1630.

Beroza, G. C., & Spudich, P. (1988). Linearized inversion for fault rupture behavior: Application to the 1984 Morgan Hill, California, earthquake. *Journal of Geophysical Research: Solid Earth*, *93*(B6), 6275–6296.

Burridge, R., & Halliday, G. (1971). Dynamic shear cracks with friction as models for shallow focus earthquakes. *Geophysical Journal International*, *25*(1-3), 261–283.

Burridge, R., & Knopoff, L. (1967). Model and theoretical seismicity. *Bulletin of the seismological society of america*, *57*(3), 341–371.

Cattania, C. (2019). Complex earthquake sequences on simple faults. *Geophysical Research Letters*, *46*(17-18), 10384–10393.

Day, S. M., Dalguer, L. A., Lapusta, N., & Liu, Y. (2005). Comparison of finite difference and boundary integral solutions to three-dimensional spontaneous rupture. *Journal of Geophysical Research: Solid Earth*, *110*(B12).

Dieterich, J. H. (1992). Earthquake nucleation on faults with rate-and state-dependent strength. *Tectonophysics*, *211*(1-4), 115–134.

Ding, X., Xu, S., Fukuyama, E., & Yamashita, F. (2024). Back-propagating rupture: Nature, excitation, and implications. *Journal of Geophysical Research: Solid Earth*, *129*(10), e2024JB029629.

Erickson, B. A., Jiang, J., Barall, M., Lapusta, N., Dunham, E. M., Harris, R., ... others (2020). The community code verification exercise for simulating sequences of earthquakes and aseismic slip (SEAS). *Seismological Research Letters*, *91*(2A), 874–890.

Flores-Cuba, J., Oral, E., Idini, B., Liang, C., & Ampuero, J. P. (2024). Mechanisms and seismological signatures of rupture complexity induced by fault damage zones in fully-dynamic earthquake cycle models. *Geophysical Research Letters*, *51*(11), e2024GL108792.

Gabriel, A.-A., Ampuero, J.-P., Dalguer, L. A., & Mai, P. (2012). The transition of dynamic rupture styles in elastic media under velocity-weakening friction. *Journal of Geophysical Research: Solid Earth*, *117*(B9). doi: https://doi.org/10.1029/2012JB009468

Huang, Y., Meng, L., & Ampuero, J.-P. (2012). A dynamic model of the frequency-dependent rupture process of the 2011 Tohoku-Oki earthquake. *Earth, planets and space*, *64*, 1061–1066.

Idini, B., & Ampuero, J.-P. (2020). Fault-zone damage promotes pulse-like rupture and back-propagating fronts via quasi-static effects. *Geophysical Research Letters*, *47*(23), e2020GL090736.

Jiang, J., Erickson, B. A., Lambert, V. R., Ampuero, J.-P., Ando, R., Barbot, S., ... others (2022). Community-driven code comparisons for three-dimensional dynamic

modeling of sequences of earthquakes and aseismic slip. *Journal of Geophysical Research: Solid Earth*, *127*(3), e2021JB023519.

Kaneko, Y., Ampuero, J.-P., & Lapusta, N. (2011). Spectral-element simulations of long-term fault slip: Effect of low-rigidity layers on earthquake-cycle dynamics. *Journal of Geophysical Research: Solid Earth*, *116*(B10).

Kaneko, Y., & Lapusta, N. (2010). Supershear transition due to a free surface in 3-D simulations of spontaneous dynamic rupture on vertical strike-slip faults. *Tectonophysics*, *493*(3-4), 272–284.

Rice, J. R. (1993). Spatio-temporal complexity of slip on a fault. *Journal of Geophysical Research: Solid Earth*, *98*(B6), 9885–9907.

Rice, J. R., & Ben-Zion, Y. (1996). Slip complexity in earthquake fault models. *Proceedings of the National Academy of Sciences*, *93*(9), 3811–3818.

Rubin, A. M., & Ampuero, J.-P. (2005). Earthquake nucleation on (aging) rate and state faults. *Journal of Geophysical Research: Solid Earth*, *110*(B11).

Uphoff, C., May, D. A., & Gabriel, A.-A. (2023). A discontinuous Galerkin method for sequences of earthquakes and aseismic slip on multiple faults using unstructured curvilinear grids. *Geophysical Journal International*, *233*(1), 586–626.

Yingdi, L., & Ampuero, J. P. (2017). Preprint: Tremor migration patterns and the collective behavior of deep asperities mediated by creep.

Table S1. Input parameters to generate fractal heterogeneities explored in this study. Corresponding fractal distributions are shown in Figure S1. (H: Hurst exponent, α: amplitude-to-wavelength ratio; g: acceleration due to gravity, 9.8 m/s^2; λ_{min} & λ_{max}: minimum and maximum wavelengths of the fractal variation, respectively; scaling factor: a constant multiplied to fractal distributions to match the order of magnitude of each parameter (Section 2.2))

Parameter	Version	Average[a.]	H	λ_{min} [km]	λ_{max} [km]	α	Scaling Factor	Random Seed
σ_n	1	50 MPa	0.7	0.75	5.0	1e-2	$1670g$	3
	2	50 MPa	0.7	0.2	1.0	1e-2	$1670g$	3
	3	50 MPa	0.7	0.5	2.5	1e-2	$1670g$	3
	4	50 MPa	0.7	0.25	2.5	1e-2	$1670g$	3
	5	50 MPa	0.7	0.5	2.5	1e-2	$1670g$	0
	6	50 MPa	0.7	0.5	2.5	1e-2	$1670g$	22
	7	50 MPa	0.7	0.5	2.5	4e-2	$1670g$	3
	d1[b.]	131 MPa	0.7	0.5	2.5	1e-2	-	3
	8	50 MPa	1.9	0.75	2.5	5e-3	$2670g$	3
	9	50 MPa	1.9	0.75	2.5	8e-3	$1670g$	3
	10	50 MPa	1.9	0.75	5.0	1e-2	$1670g$	3
	11	50 MPa	1.9	0.2	1.0	1e-2	$1670g$	3
	12[c.]	50 MPa	$\sim$1.9	$\sim$0.5	$\sim$2.5	-	-	-
	13	50 MPa	1.9	0.5	2.5	1.2e-2	$1670g$	12
	d2[b.]	131 MPa	1.9	0.5	2.5	1e-2	-	3
$(a-b)$	1	-0.004	0.7	0.5	2.5	1e-2	1.25e-5	3
	1m[d.]	-0.0037	-	-	-	-	-	-
	2	-0.004	0.7	0.5	2.5	1e-2	2.1e-5	3
	3	-0.004	1.9	0.5	2.5	1e-2	3.2e-6	3
	4	-0.004	1.9	0.5	2.5	1e-2	1.6e-5	3
D_{RS}	1	2 mm	0.7	0.5	2.5	1e-2	1.5e-6	3
	2[e.]	10 mm	0.7	0.5	2.5	1e-2	7.5e-6	3
	3	4 mm	1.9	0.5	2.5	1e-2	3.2e-6	3
	4	2 mm	1.9	0.5	2.5	1e-2	1.6e-6	3
	5	2 mm	1.9	0.5	2.5	1e-2	1.3e-6	50
	6[f.]	10 mm	1.9	0.5	2.5	1e-2	8.0e-6	3

[a.] Value below 2 km for σ_n; Value within the velocity-weakening seismogenic zone (2 km - 12 km) for $(a-b)$.

[b.] Depth-dependent effective normal stress models.

[c.] Not strictly a fractal distribution found by trial-and-error. See Section 3.2.

[d.] Modified from ver.1 to match the strength of the N3R1 model. See Section 3.2.

[e.] Identical to multiplying a factor of 5 to the version 1.

[f.] Identical to multiplying a factor of 5 to the version 4.

Table S2. List of all explored models in this study. Dash marks indicate the model does not incorporate fractal variation in the given parameter (or does not include a low-rigidity fault zone) and the parameter follows the base value shown in Table 1 of the main text. Models are named by the combination of parameter name (N: effective normal stress, Nd: depth-dependent effective normal stress, R: rate-and-state parameter $(a-b)$, D: characteristic state evolution distance D_{RS}, and FZ: low-velocity fault zone) and the version of the fractal model (Table S1). CCS: Combined Complexity Score.

	Model Name	σ_n [MPa]	$a-b$	D_{RS} [mm]	μ [GPa]	μ_{FZ} [GPa]	CCS
Single Heterogeneity	N1	ver. 1	-	-	32	-	0.0
	N2	ver. 2	-	-	32	-	0.0
	N3	ver. 3	-	-	32	-	0.0
	N4	ver. 4	-	-	32	-	0.0
	N5	ver. 5	-	-	32	-	0.0
	N6	ver. 6	-	-	32	-	0.0
	N7	ver. 7	-	-	32	-	0.2
	N8	ver. 8	-	-	32	-	0.0
	N9	ver. 9	-	-	32	-	0.0
	N10	ver. 10	-	-	32	-	0.0
	N11	ver. 11	-	-	32	-	0.0
	N11-2	ver. 11	-	1.5	32	-	0.4
	N11-3	ver. 11	-	0.8	32	-	0.2
	N12	ver. 12	-	-	32	-	0.2
	N12-2	ver. 12	-	1.5	32	-	0.2
	N12-3	ver. 12	-	2.0	10	-	0.5
	N13	ver. 13	-	-	32	-	0.0
	Nd1	ver. d1	-	-	32	-	0.0
	Nd2	ver. d2	-	-	32	-	0.0
	R1	-	ver. 1	2.0	32	-	0.9
	R1m	-	ver. 1m	-	15	-	0.3
	R2	-	ver. 2	-	32	-	0.8
	R3	-	ver. 3	1.5	32	-	0.2
	R4	-	ver. 4	2.0	32	-	0.8
	D1	-	-	ver. 1	32	-	0.2
	D3	-	-	ver. 3	32	-	0.0
	D3-2	-	-	ver. 3	10	-	0.2
	D4	-	-	ver. 4	32	-	0.3
	D4-2	-	-	ver. 4	10	-	*
	D5	-	-	ver. 5	32	-	0.9
	D5-2	-	-	ver. 5	10	-	0.6

* Too short to estimate complexity score.

Table S2. (continued)

	Model Name	σ_n [MPa]	$a-b$	D_{RS} [mm]	μ [GPa]	μ_{FZ} [GPa]	CCS
Double Heterogeneities	N3R1	ver. 3	ver. 1	-	15	-	0.7
	N3R1-2	ver. 3	ver. 1	-	32	-	1.1
	N3D1	ver. 3	-	ver. 1	20	-	0.2
	N10R4	ver. 10	ver. 4	-	15	-	0.7
	N11R4	ver. 11	ver. 4	-	15	-	0.9
	N12R4	ver. 12	ver. 4	-	15	-	0.9
	N12D3	ver. 12	-	ver. 3	10	-	0.2
	N12D4	ver. 12	-	ver. 4	20	-	0.2
	R4D3	-	ver. 4	ver. 3	20	-	0.8
	R4D4	-	ver. 4	ver. 4	20	-	0.9
Triple Heterogeneities	N3R1D1	ver. 3	ver. 1	ver. 1	20	-	1.0
	N3R1D1-2	ver. 3	ver. 1	ver. 1	32	-	1.1
	N3R2D1	ver. 3	ver. 2	ver. 1	20	-	0.8
	N3R1D2	ver. 3	ver. 1	ver. 2	20	-	0.8
	N3R1D2-S**	ver. 3	ver. 1	ver. 2	20	-	1.0
	N12R3D3	ver. 12	ver. 3	ver. 3	10	-	0.0
	N12R4D3	ver. 12	ver. 4	ver. 3	10	-	1.2
	N12R4D4	ver. 12	ver. 4	ver. 4	20	-	2.9
	N12R4D4-2	ver. 12	ver. 4	ver. 4	32	-	0.7
	N12R4D6	ver. 12	ver. 4	ver. 6	20	-	0.6
	N12R4D6-S**	ver. 12	ver. 4	ver. 6	20	-	0.2
Low-rigidity Fault Zone	FZ	-	-	-	32	10	0.2
	N12FZ	ver. 12	-	-	32	10	0.2
	N3D1FZ	ver. 3	-	ver. 1	32	20	0.0
	N12D4FZ	ver. 12	-	ver. 4	32	20	0.2

** Slip law models

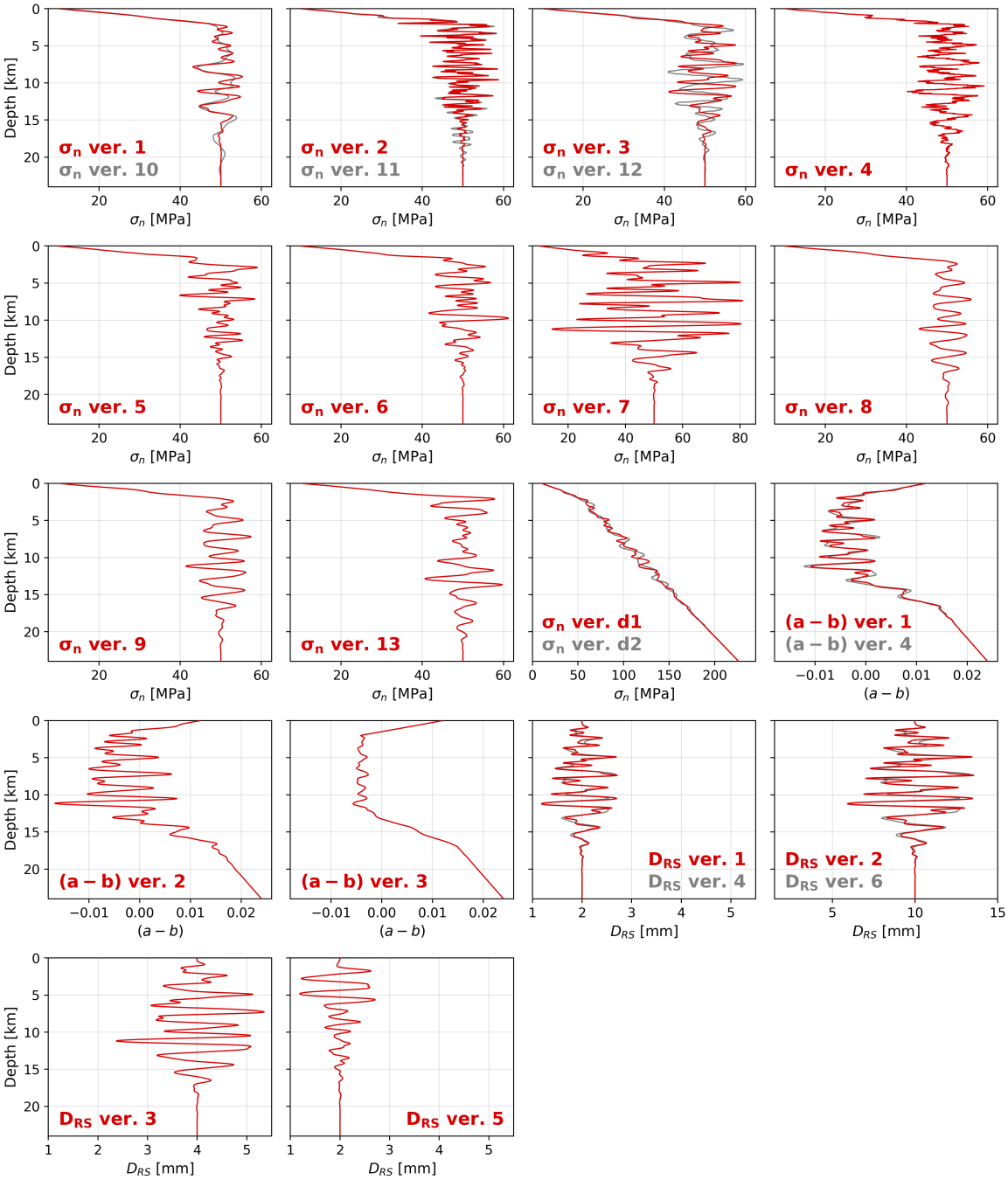

Figure S1. All fractal heterogeneity models explored in this study. Version numbers of each heterogeneity follow those in Table S1. Models that share the same statistical properties except Hurst exponent values are plotted in the same panel, as red lines ($H = 0.7$) and grey lines ($H = 1.9$).

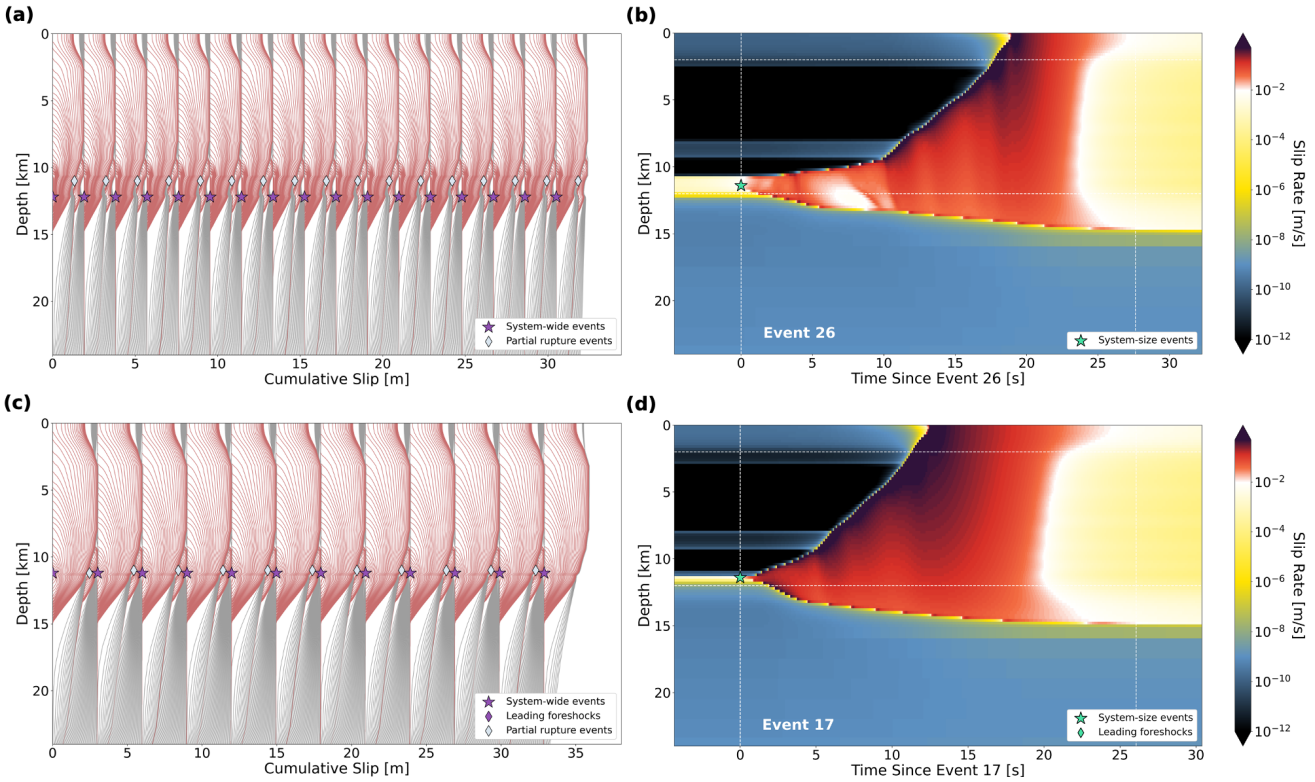

Figure S2. Comparison of models (a) with (model N12D4FZ) and (b) without (model N12D4) a low-rigidity fault zone using $H = 1.9$ (see Section 3.2 of the main text). (a, c) Cumulative slip evolution of models (a) N12D4FZ and (c) N12D4. (b, d) Zoom-in of one of the system-size events (event 26 in model N12D4FZ and event 17 in model N12D4) in each model. Multiple slip pulses with some back-propagating rupture fronts are observed in model N12D4FZ (panel (b)). Green stars indicate the hypocenter locations of system-size earthquakes.

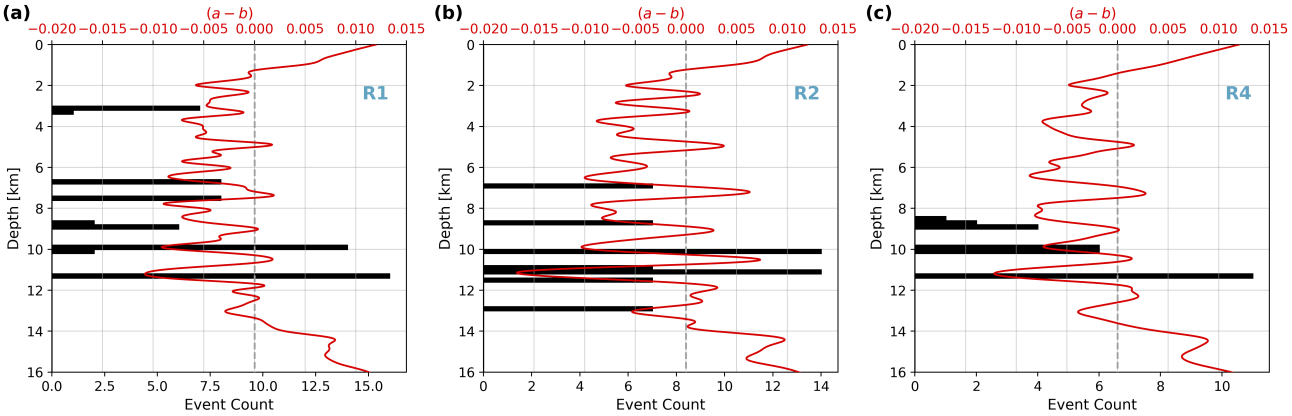

Figure S3. Spatial distribution of $(a - b)$ heterogeneity versions 1, 2, and 4 (red lines) and histograms of earthquake hypocenter depths in associated models R1, R2, and R4 (black bars).

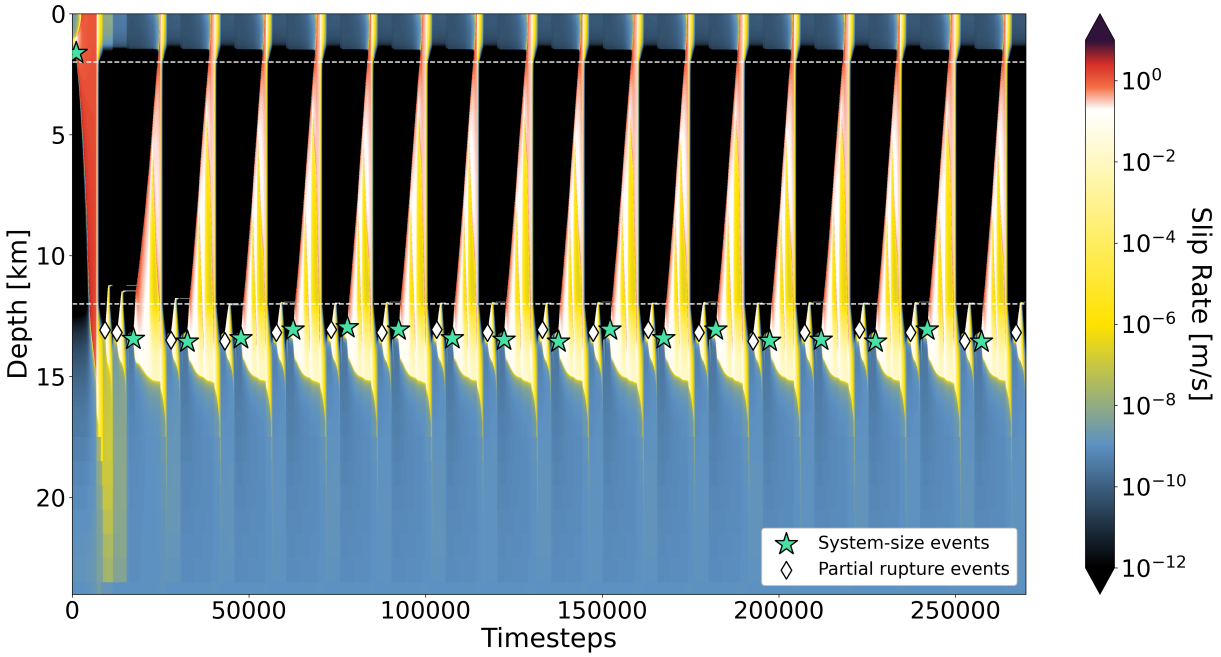

Figure S4. Spatiotemporal evolution of slip rate of a homogeneous model with a uniform $W/L_\infty = 251$ at all depths, comparable to the maximum W/L_∞ value of model N12R4D4. Green stars and white diamonds indicate the hypocenter locations of system-size earthquakes and partial rupture events, respectively.

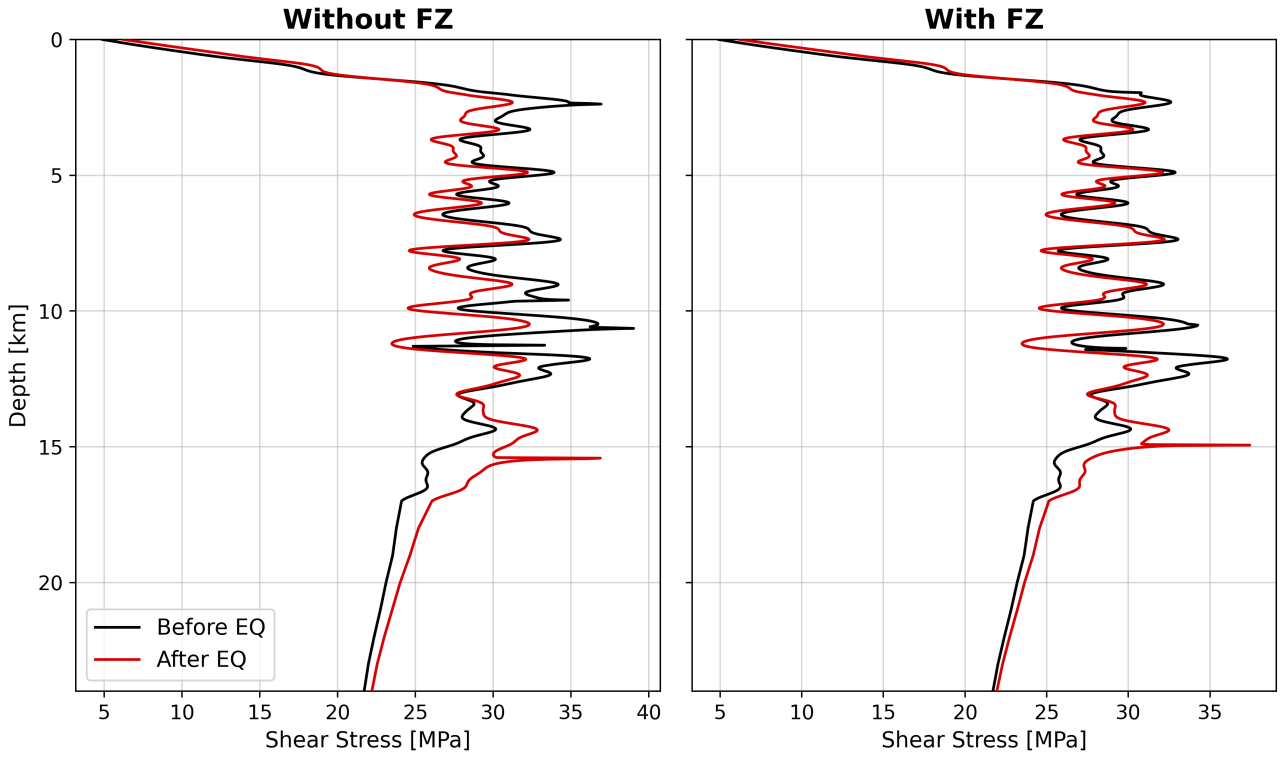

Figure S5. Shear stress 1 hour before (black) and after (red) a system-size earthquake in models with (right; model N3D1FZ) and without (left; model N3D1) the low-rigidity fault zone.

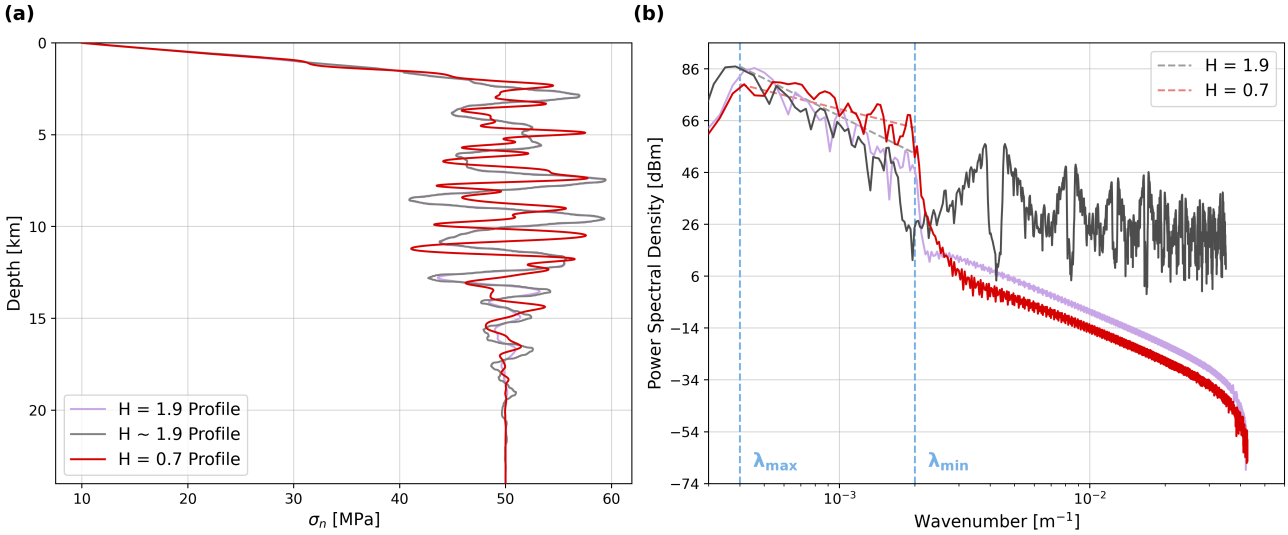

Figure S6. Comparison of not strictly fractal σ_n heterogeneity with $H \sim 1.9$ (version 12; grey lines) with σ_n heterogeneity version 3, which has the same limiting wavelengths as version 12 but is strictly fractal with $H = 0.7$. For comparison, a strictly fractal σ_n heterogeneity sharing the same limiting wavelengths and H value as version 12 (light purple line) is shown in panel (a).

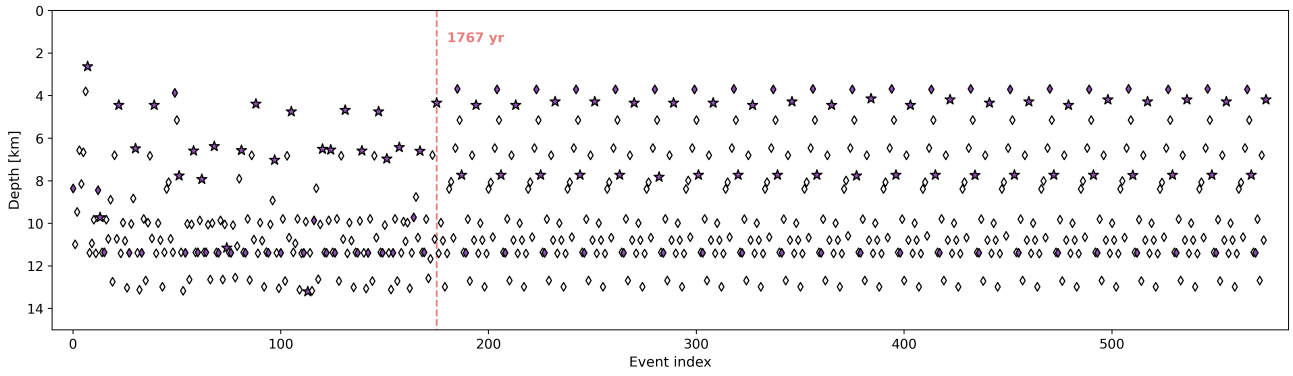

Figure S7. Hypocenter depth distribution for all earthquakes in model N12R4D4. A transition from an aperiodic to a cycle-invariant regime occurs after ∼1750 yr of simulation time (pink dashed line). Purple stars, purple diamonds, and white diamonds indicate the hypocenter locations of system-size earthquakes, leading foreshocks, and partial rupture events, respectively.

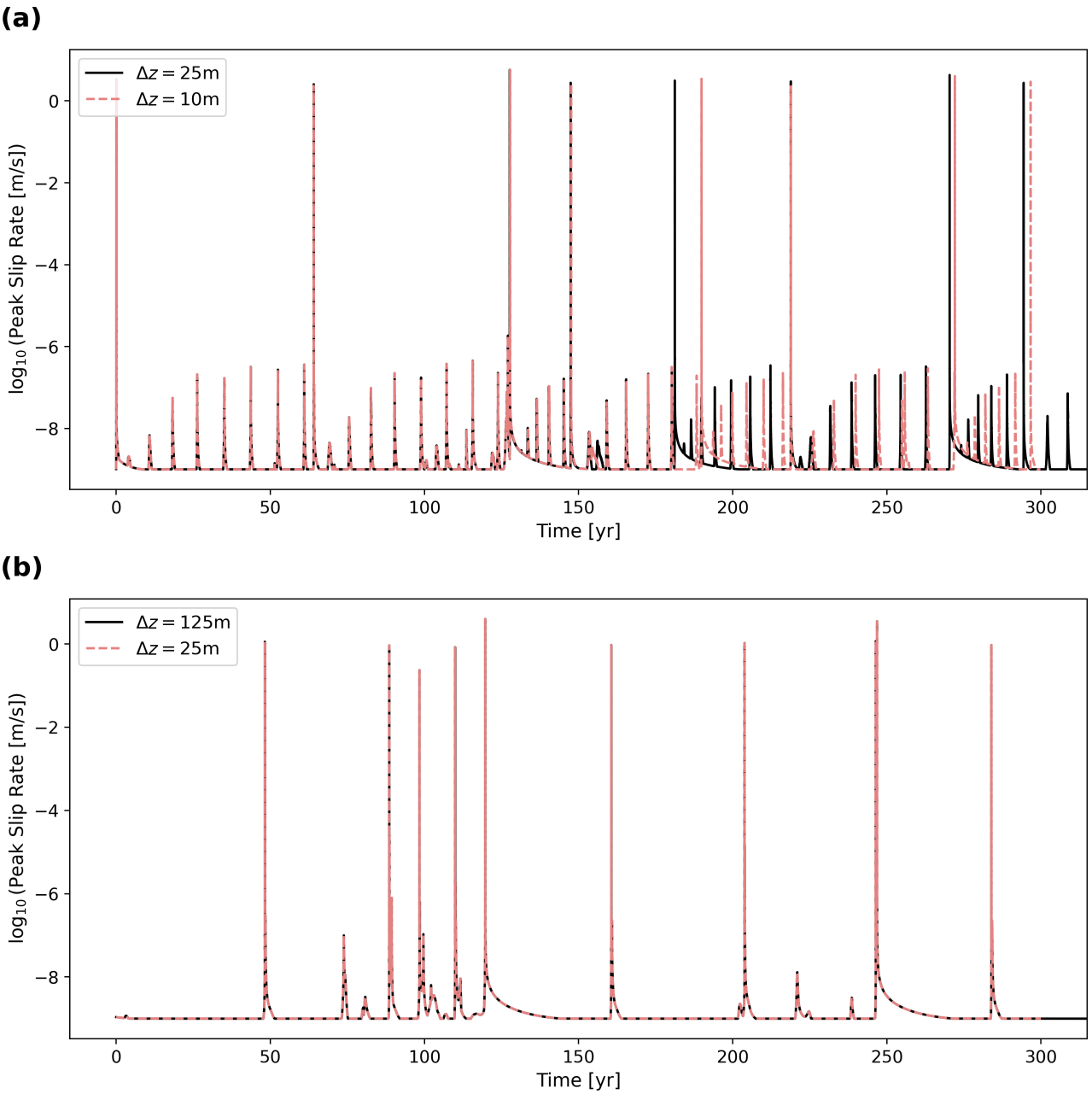

Figure S8. Comparison of peak slip rate evolution resulting from different mesh sizes. (a) Peak slip rate evolution of model N12R4D4 using $\Delta z = 25$ m (black solid line) and $\Delta z = 10$ m (pink dashed line). The two models agree well before ∼150 yr. (b) Peak slip rate evolution of model N12R4D6 using $\Delta z = 125$ m (black solid line) and $\Delta z = 25$ m (pink dashed line). The two models agree well for ∼300 yr.

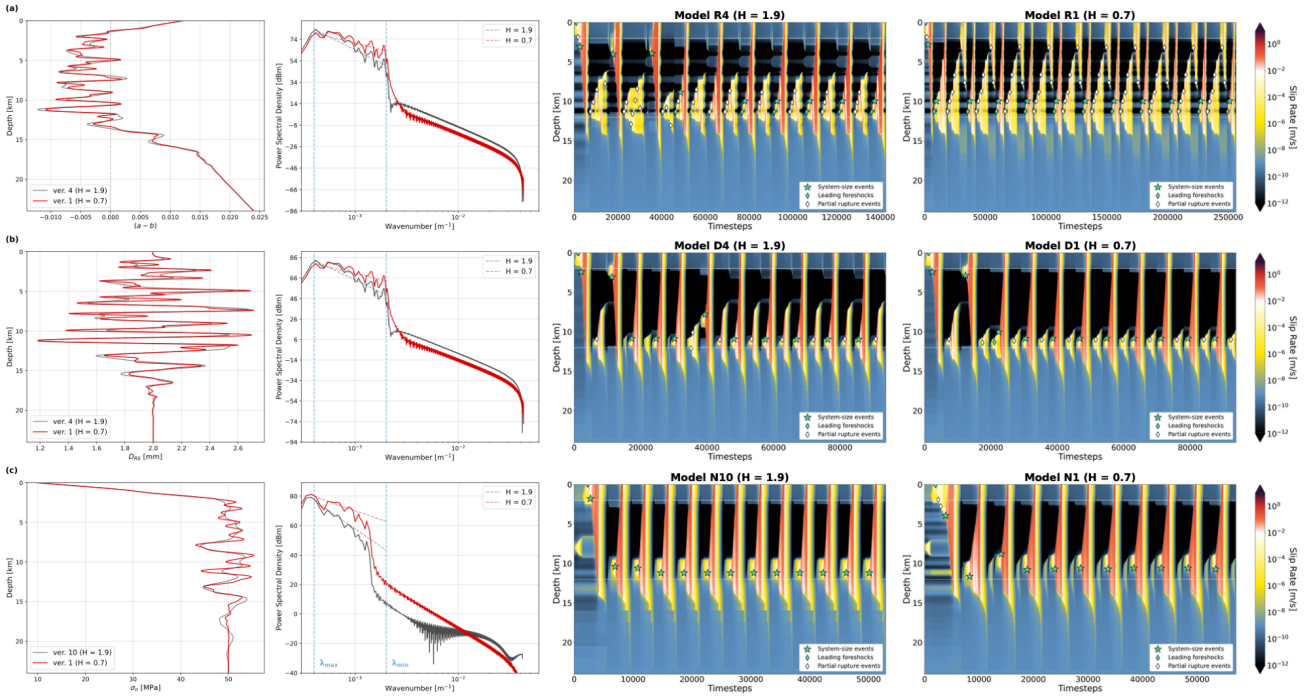

Figure S9. Comparison of fractal heterogeneities in (a) $(a-b)$, (b) D_{RS}, and (c) σ_n with $H = 1.9$ (grey) and $H = 0.7$ (red). The first and second columns show the depth distribution of each fractal heterogeneity and power spectral density as a function of wavenumber (Eq. (7) in the manuscript), respectively. Note the slope of $2H + 1$ in the power spectral density (light grey and pink dashed lines) within the limiting wavelengths (blue vertical lines). The third and fourth columns compare the spatiotemporal evolution of slip rate obtained from each fractal heterogeneity with $H = 1.9$ and $H = 0.7$, respectively. All plots show 700 yr of slip rate evolution.

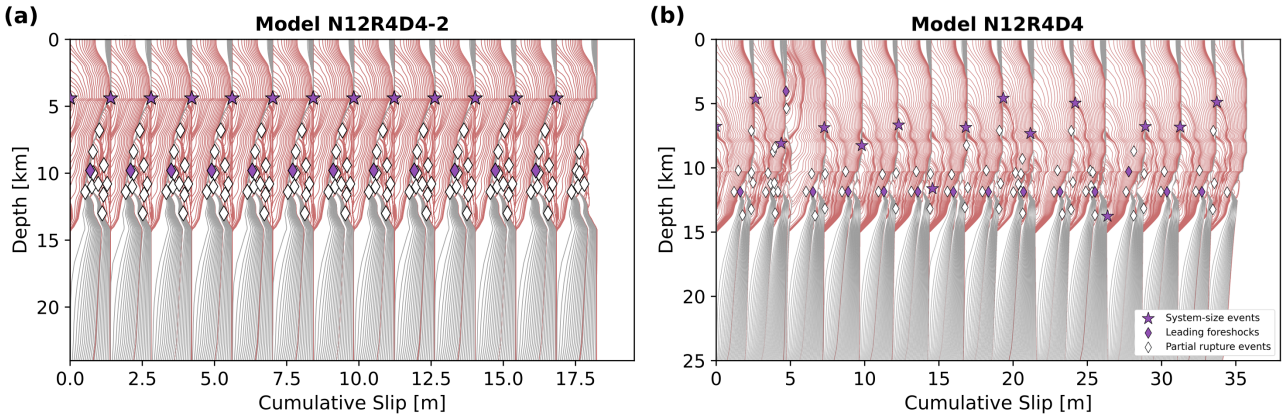

Figure S10. Comparison of cumulative slip evolution of models (a) N12R4D4-2 ($\mu = 32$ GPa) and (b) N12R4D4 ($\mu = 20$ GPa).